Effects of tropical sea surface temperature variability on Northern Hemisphere tropical cyclone genesis

Shuo Li[1], Wei Mei[1*] and Shang-Ping Xie[2]

1. Department of Earth, Marine and Environmental Sciences, University of North Carolina at Chapel Hill, Chapel Hill, North Carolina
2. Scripps Institution of Oceanography, University of California, San Diego, La Jolla, California

*Corresponding author: Wei Mei, wmei@email.unc.edu

Abstract: This study quantifies the contributions of tropical sea surface temperature (SST) variations during the boreal warm season to the interannual-to-decadal variability in tropical cyclone genesis frequency (TCGF) over the Northern Hemisphere ocean basins. The first seven leading modes of tropical SST variability are found to affect basin-wide TCGF in one or more basins, and are related to canonical El Niño–Southern Oscillation (ENSO), global warming (GW), the Pacific Meridional Mode (PMM), Atlantic Multidecadal Oscillation (AMO), Pacific Decadal Oscillation (PDO) and Atlantic Meridional Mode (AMM). These modes account for approximately 58%, 50% and 56% of the variance in basin-wide TCGF during 1969–2018 over the North Atlantic (NA), Northeast Pacific (NEP) and Northwest Pacific (NWP), respectively. The SST effect is weak on TCGF variability in the North Indian Ocean. The dominant SST modes differ among the basins: ENSO, the AMO, AMM and GW for the NA; ENSO and the AMO for the NEP; and the PMM, interannual AMO and GW for the NWP. A specific mode may have opposite effects on TCGF in different basins, particularly between the NA and NEP. Sliding-window multiple linear regression analyses show that the SST effects on basin-wide TCGF are stable in time in the NA and NWP, but strengthen after the mid-1970s in the NEP. The SST effects on local TC genesis and occurrence frequency are also explored, and the underlying physical mechanisms are examined by diagnosing a genesis potential index and its components.

1. Introduction

Around 70% of global tropical cyclones (TCs) are in the Northern Hemisphere [including the North Atlantic (NA), Northeast Pacific (NEP), Northwest Pacific (NWP) and North Indian Ocean (NIO)]. Their genesis is strongly modulated by the large-scale atmospheric environment in which the storms are embedded and by the surface temperature of the underlying ocean from which the storms extract energy for development (e.g., Gray 1968; Zehr 1992; Emanuel 2003, 2018; Knutson et al. 2008, 2010; Tory and Frank 2010; Vecchi et al. 2011; Nolan and McGauley 2012). The large-scale atmospheric environment is also shaped by the surface temperature of the ocean, particularly in the tropics (e.g., Palmer and Mansfield 1984; Lau 1985; Kucharski et al. 2008; Xie et al. 2016; Wang 2019). Thus, a good understanding and an accurate prediction of tropical sea surface temperatures (SSTs) can improve the prediction of seasonal TC genesis frequency (TCGF). Indeed, year-to-year variations in TCGF have been linked to various modes of SST variability, such as El Niño–Southern Oscillation (ENSO), the Atlantic Meridional Mode (AMM), Atlantic Multidecadal Oscillation (AMO), Pacific Decadal Oscillation (PDO), Pacific Meridional Mode (PMM) and Indian Ocean Basin (IOB) mode (e.g., Camargo et al. 2010).

Climate modes that have been identified to influence NA TCGF include ENSO, the AMM and AMO. SST anomalies in the equatorial Pacific associated with El Niño displace the atmospheric convection eastward in the tropical Pacific, which weakens the Walker circulation and strengthens westerly in the upper troposphere over the tropical NA and Caribbean Sea. The enhanced westerly increases vertical wind shear in these regions and thereby suppresses TC genesis in the NA (e.g., Gray 1984; Goldenberg and Shapiro 1996; Landsea et al. 1999; Aiyyer and Thorncroft 2006; Klotzbach 2011). Meanwhile, El Niño tends to stabilize the air column in the tropical NA by warming up the upper troposphere (Tang and Neelin 2004; Klotzbach 2011)

and reduce tropospheric humidity (Camargo et al. 2007), both of which also discourage TC genesis in this region. In contrast, NA TC genesis is active during a positive phase of the AMM, which features warmer-than-normal SSTs over the tropical NA and a northward shift of the Intertropical Convergence Zone (Xie and Carton 2004; Chiang and Vimont 2004). The anomalously warm SSTs in the tropical NA tend to reduce sea level pressure and enhance deep convection, resulting in an anomalous atmospheric circulation that decreases vertical wind shear and increases low-level vorticity. All these favor TC genesis in the NA (Xie et al. 2005; Kossin and Vimont 2007; Vimont and Kossin 2007). The AMO has nearly the same effects as the AMM but is more prominent on multidecadal timescales, and has contributed to the above-normal TC activity since the mid-1990s when it switched to a positive phase (Landsea et al. 1999; Goldenberg et al. 2001; Klotzbach 2011).

In the NEP, TC genesis is modulated by SSTs associated with climate modes in both the Pacific and Atlantic. ENSO tends to influence TC genesis in the western NEP via changes in local SSTs, convective activity and relative humidity, with higher TC genesis during El Niño years (Watterson et al. 1995; Clark and Chu 2002; Camargo et al. 2008; Klotzbach and Blake 2013; Jien et al. 2015). ENSO effect is weak on TCGF in the eastern NEP (Collins 2010; Caron et al. 2015; Jien et al. 2015). As a result, in the NEP El Niño shifts TC genesis location westward (Irwin and Davis 1999) with only a modest difference in basin-wide TCGF between El Niño and non-El Niño years (Whitney and Hobgood 1997). Meanwhile, SST anomalies associated with the AMO and in the NA subtropical gyre can modulate NEP TC genesis on both interannual and decadal timescales, with more TCs forming in the NEP when NA SSTs are below normal. These Atlantic factors operate by changing upper-level easterly winds and thus vertical wind shear in the NEP (Camargo et al. 2007, 2008; Wang and Lee 2009; Caron et al. 2015; Zhang and Wang 2015). In short, the effects of ENSO and NA SSTs on the NEP TC genesis are opposite to those on NA TC genesis,

which can largely explain the observed negative correlation in TC counts between the two basins (Elsner and Kara 1999; Wang and Lee 2009; Collins 2010; Caron et al. 2015). In addition, the PMM may also exert a strong influence on NEP TC genesis and occurrence frequency, particularly in the western portion (Collins et al. 2016; Murakami et al. 2017; Wood et al. 2019).

The factors governing TC genesis in the NWP mainly include ENSO, the PMM, and SST anomalies in the Indian and Atlantic Oceans. ENSO tends to generate more TCs in the southeastern quadrant of the NWP and fewer TCs in the northwestern quadrant during its positive phase, without significantly altering basin-wide TC counts (e.g., Chan 1985; Wang and Chan 2002; Choi et al. 2015). Such a displacement in genesis location is associated with increased low-level vorticity and reduced vertical wind shear in the southeastern NWP (e.g., Wang and Chan 2002; Clark and Chu 2002), tied to an eastward expansion of the monsoon trough, and decreased mid-level humidity near the Asian continent (Camargo et al. 2007). Since the 1990s, a different flavor of El Niño has occurred frequently with the warm anomaly peaking in the central equatorial Pacific (e.g., Yeh et al. 2009; Yu et al. 2012). This central-Pacific (CP) El Niño (also called El Niño modoki; Ashok et al. 2007; Kao and Yu 2009) favors higher basin-wide TCGF (e.g., Chen and Tam 2010; Kim et al. 2011; Mei et al. 2015; Wu et al. 2018; Zhao and Wang 2019) by exciting conducive atmospheric condition (e.g., cyclonic circulation anomaly in the lower troposphere) over much of the basin. More recently, the PMM, which features a meridional dipole pattern of SST anomalies and sometimes may promote the initiation of CP or canonical El Niño (e.g., Larson and Kirtman 2014; Capotondi and Sardeshmukh 2015; Amaya 2019), has been linked to the variations in NWP TCGF: a positive PMM encourages more TC genesis primarily by changes in dynamical factors (e.g., decreased vertical wind shear; Zhang et al. 2016; C. Liu et al. 2019). SST anomalies outside the Pacific also exert influences on NWP TCGF (Wu et al. 2020). Anomalous SST warming in the

94 tropical Indian Ocean during post-El Niño summers (Xie et al. 2009) can significantly suppress
95 NWP TCs by triggering an anomalous anticyclone over the NWP (e.g., Du et al. 2011; Zhan et al.
96 2011; Tao et al. 2012; Ha et al. 2015). Above-normal SSTs in the tropical NA may also discourage
97 NWP TC genesis via their effects on SSTs of the Indian Ocean and subtropical North Pacific and
98 on the Walker circulation (e.g., Ham et al. 2013; Huo et al. 2015; Yu et al. 2016; Gao et al. 2018;
99 Zhang et al. 2018).

100 ENSO is the only climate mode that has been linked to the interannual variations in TCGF
101 over the NIO. In the Bay of Bengal, fewer TCs form in the months of May and November under
102 El Niño conditions, in response to reduced low-level relative vorticity, increased vertical wind
103 shear and reduced relative humidity; the effect is insignificant in other months (Singh et al. 2000;
104 Felton et al. 2013). The effect of ENSO on TCGF in the Arabian Sea is very weak (Singh et al.
105 2000). Consistently, the genesis potential indices (GPIs), reanalysis products and dynamical
106 models (either coupled or atmosphere-only) cannot reproduce the observed year-to-year TCGF
107 variations over the NIO, although some of them are able to capture the climatological seasonal
108 cycle of TC genesis (Camargo et al. 2007; Zhao et al. 2009; Camp et al. 2015). These results
109 suggest that either the NIO TCGF is unpredictable or other factors (including those related to the
110 underlying SSTs) await to be identified (e.g., Murakami et al. 2017).

111 As stated above, several tropical SST factors have been identified to affect TCGF
112 variability, and previous studies tend to focus on a small subset of these factors. It is unclear
113 whether these SST factors are independent. Moreover, their relative contributions to TCGF
114 variations remain to be quantified and the underlying physical mechanisms need to be explored.
115 To address these issues and quantify the integrated effects of the tropical SSTs on TC activity, we
116 take the tropical oceans as a whole, and first obtain the leading modes that effectively and

thoroughly represent tropical SST variations via a systematic and objective decomposition. Specifically, we extract the leading modes in the tropical SSTs during the boreal warm season (i.e., June–November) using an empirical orthogonal function (EOF) analysis (section 3). We then quantify and compare the individual and combined effects of these distinct SST modes on TC genesis and occurrence frequency in the four basins of the Northern Hemisphere (section 4.1). Insights into how tropical SSTs modulate TC genesis in different basins are gained through a diagnosis and decomposition of a GPI (section 4.2). Lastly, we examine the potential decadal changes in these tropical SST effects (section 4.3).

2. Data and Methods

2.1 Data

Monthly SSTs of the boreal warm season (i.e., June–November, the period when nearly 90% of Northern Hemisphere TCs form) during 1951–2018 from the Hadley Centre SST dataset (Rayner et al. 2003) are used to study the interannual-to-decadal variations in tropical SSTs during the Northern Hemisphere TC peak season. Monthly atmospheric variables during June–November from the Japanese 55-year Reanalysis (JRA-55; Kobayashi et al. 2015) are adopted to connect variations in TCGF to those in tropical SSTs and understand the underlying physical mechanisms. Using the Extended Reconstructed Sea Surface Temperature version 5 (ERSSTv5; Huang et al. 2017) dataset and the National Centers for Environmental Prediction and the National Center for Atmospheric Research (NCEP/NCAR; Kalnay et al. 1996) Reanalysis 1 dataset produces results very similar to those obtained using the Hadley Centre SST and JRA-55 datasets.

TC data for the NA and NEP (east of 180° longitude) basins are from the National Hurricane Center best-track dataset (Landsea and Franklin 2013), and for the NIO are from the Joint Typhoon Warning Center (JTWC) best-track dataset (Chu et al. 2002). For the NWP basin

(west of 180° longitude), because of the discrepancies in TC frequency among different data sources we use three best-track datasets respectively from the Shanghai Typhoon Institute of the China Meteorological Administration, Japan Meteorological Agency and JTWC (e.g., Ren et al. 2011; Schreck et al. 2014; Barcikowska et al. 2017). All these best-track datasets provide the location and intensity of TCs at 6-hour intervals. TCs with at least tropical storm intensity during 1951–2018 are considered in this study, but since satellite measurements became available after the late 1960s, only those over the most recent 50 years (i.e., 1969–2018) are used in the regression analysis (section 4) given the higher quality of the data (e.g., Chang and Guo 2007; Landsea et al. 2010; Vecchi and Knutson 2011). For the NIO, only TC data since 1977 are used because of the inconsistencies between JTWC Archive data and the data published in JTWC's Annual Tropical Cyclone Reports (Chu et al. 2002). It is worth noting that the short duration tropical storms increased since 2000 in North Atlantic while medium- to long-lived storms have increased little, which has been attributed to changes in observing capabilities (Landsea et al. 2010; Villarini et al. 2011). To account for these biases in TC measurements, we consider only TCs with a duration of at least two days.

2.2 Methods

An EOF analysis is employed to extract the leading modes of interannual-to-decadal variability in boreal warm-season-averaged SSTs over the tropics (30°S–30°N) during 1951–2018. Multiple linear regression analysis is used to build statistical models linking TCGF in individual basins to the principle components (PCs) of the leading SST modes. Simple linear regression and correlation analyses are applied to identify the atmospheric conditions that physically connect tropical SST variations with local TC genesis and occurrence frequency, with the significance level of the results estimated by the standard two-tailed Student's *t*-test.

TC genesis frequency is calculated as the total number of TCs forming in each basin or each 8°×8° grid on a yearly basis. TC occurrence frequency (also called track density) is calculated as the total number of TC days each basin or each 8°×8° grid experiences on a yearly basis. The large grid (i.e., 8°×8°) is used in order to reduce the noise level and using a smaller grid (e.g., 5°×5° or 6°×6°) gives similar results. A GPI, denoting the favorability of the large-scale environment in which TCs develop, is calculated following Emanuel (2010) as:

$$\mathrm{GPI} = \frac{a|\eta|^3[\max(V_{\mathrm{PI}}-35,0)^2]}{\chi^{4/3}(25+V_{\mathrm{sh}})^4}, \qquad \text{Eq. (1)}$$

where a is a constant and set to be 10^{16} in this study, η is the 850-hPa absolute vorticity, V_{PI} is the TC potential intensity, χ is the 600-hPa entropy deficit and V_{sh} is the magnitude of the 250–850-hPa wind shear vector (see also Korty et al. 2012; Tang and Emanuel 2012).

3. Tropical SST modes

The first seven modes (M1–M7) extracted via the EOF analysis totally account for 79.9% of the variance in tropical SST anomalies, with each explaining 39.6%, 20.2%, 7.0%, 3.8%, 3.4%, 3.2%, and 2.7%, respectively. These tropical SST modes can be linked to well-known modes of climate variability, although M4 to M7 may not be well separated based on North's rule of thumb (North et al. 1982) presumably because of (1) the short study period and (2) the locality of these SST modes; indeed, Messié and Chavez (2011) were able to obtain modes that are similar but significant with 100-year monthly data. Except one mode tied to the secular global warming trend, three modes are dominated by variations in the Pacific and the other three by variations in the Atlantic. Collectively, these SST modes well represent the signal in tropical SST variations. Before quantifying their combined effects on the Northern Hemisphere TC activity, we first describe these modes individually. The left and right panels of Fig. 1 show their spatial patterns and principal components (PC1–PC7), respectively.

M1 explains 39.6% of the tropical SST variance, and features the classical ENSO pattern with the strongest variability in the central and eastern equatorial Pacific (Fig. 1a). Its PC (i.e., PC1) is highly correlated with Niño indices (e.g., $r = 0.93$ for the Niño-3 index during 1951–2018; Fig. 1b) and captures strong El Niño events (e.g., in 1997 and 2015). The spatial pattern of this mode resembles that of the leading mode extracted from global detrended SST anomalies of 1910–2009 in Messié and Chavez (2011), indicating the robustness of this mode. Meanwhile, an Indian Ocean Dipole (IOD)-like pattern exists over the Indian Ocean (Fig. 1a) and PC1 is significantly correlated with the IOD index ($r = 0.57$; Fig. 1b), consistent with previous studies suggesting that ENSO and the IOD are coherently linked (e.g., Ju et al. 2004; Y. Liu et al. 2019).

M2 features a pattern of global warming with strong warming occurring during the past seven decades in the Atlantic Ocean, Indian Ocean and western portion of the Pacific Ocean. Weak cooling occurs in the equatorial eastern Pacific Ocean and Southern Ocean (Fig. 1c). PC2 shows a strong upward trend and is highly correlated with the global mean SST during 1951–2018 ($r = 0.74$; Fig. 1d). It is worth noting that, when individual basins are considered, PC2 is significantly correlated with the Atlantic Niño index ($r = 0.62$) and IOB index ($r = 0.71$) during 1951–2018, implying the covariations of SSTs in the tropical Atlantic and Indian Oceans. This mode shares similarities with a combination of EOF modes 1, 2 and 3 in Dong and Zhou (2014) and the second mode of tropical Pacific SST variability shown in Jiang and Zhu (2018). We further separated PC2 into interannual and decadal components and then regressed them against global SST anomalies (not shown). It is found that the interannual component is associated with La Niña and significantly correlated with PC1 ($r = -0.54$). The regressed SST pattern of the low-frequency component resembles that of Dong and Zhou (2014). It is unclear why part of ENSO variability is embedded in this global warming mode.

M3 resembles the PMM, which is the second leading mode of coupled ocean-atmosphere variability in the Pacific and characterized by out-of-phase SST variations over the north tropical Pacific and eastern equatorial Pacific (Fig. 1e; Chiang and Vimont 2004; Amaya 2019). The correlation coefficient between PC3 and the PMM index defined by Chiang and Vimont (2004) is 0.90 for the period of 1951–2018 (Fig. 1f). During a positive phase, the warm anomaly extends to the central equatorial Pacific and cold anomaly exists over eastern and western (though insignificant for the latter) equatorial Pacific, thus this mode also shares some similarities with the CP ENSO (Ashok et al. 2007; Kao and Yu 2009); the correlation coefficient between PC3 and the El Niño modoki index (EMI) is 0.83 during 1951–2018 (Fig. 1f).

M4 exhibits some typical characteristics of the AMO, and features anomalous warming in the tropical and high-latitude North Atlantic and in the subtropical North Pacific, and cold anomaly over the subtropical South Atlantic and Indian Ocean (Fig. 1g). PC4 primarily displays low-frequency variations, and its correlation coefficient with the detrended AMO index is 0.52, with the two time series differing mainly during the 1960s and early 1970s (Fig. 1h). When both time series are filtered using an 8-year low-pass filter, their correlation coefficient rises to 0.65 (not shown).

M5 is characterized primarily by a dipole pattern of SST variations over the mid-latitude western and eastern North Pacific (Fig. 1i). This mode is very similar to the third mode of the global SST variability depicted in Messié and Chavez (2011), and both differ from the conventional PDO, which also exhibits strong SST variability in the equatorial Pacific. The correlation coefficient between PC5 and the PDO index of June–November and of April–July during 1951–2018 is 0.46 and 0.62 (Fig. 1j), respectively. An east-west dipole pattern also exists over the low-latitude South Indian Ocean (Fig. 1i).

M6 resembles the AMM, with SST changes in the tropical NA opposite to those in the tropical South Atlantic (Fig. 1k). The correlation coefficient between PC6 and the AMM index defined based on the coupled ocean-atmosphere variability (Chiang and Vimont 2004) is 0.59 during 1951–2018 (Fig. 1l). The spatial pattern of this mode is similar to the opposite phase of the sixth mode in Messié and Chavez (2011), where it is described as the Atlantic Niño; the correlation coefficient between PC6 and the Atlantic Niño index is -0.59 (not shown).

M7 features anomalous SST warming in the NA (Fig. 1m), similar to the pattern of M4 but primarily on interannual timescales; the correlation coefficient between PC7 and the interannual component of the AMO index is 0.62 during 1951–2018 (Fig. 1n). High loadings are also over the subtropical NEP, where significant cooling is observed (Fig. 1m). This cooling can be linked to the warming in the tropical NA via inter-basin ocean-atmosphere interactions (Ham et al. 2013): SST warming over the tropical NA generates an anomalously cyclonic circulation in the lower troposphere over the subtropical NEP as a Gill-type Rossby-wave response, and the northerlies on the west flank of the anomalous cyclone produce SST cooling via both enhanced wind speed and cold advection from higher latitudes.

The above SST modes are statistically independent over the 68-year period. Because of the limited realizations, especially for interdecadal variations and unfolding global warming, uncertainty remains as to the detailed spatial structure of M2. Various techniques have been attempted to ascertain the global warming pattern (e.g., Tokinaga et al. 2012; Chen and Wallace 2016). These caveats aside, the EOF is an effective and efficient method to decompose SST variations into a small number of modes. Using the ERSSTv5 dataset produces very similar results (Fig. S1), confirming the robustness of the identified tropical SST modes. We note that the PCs of some of the extracted modes (particularly modes 4–7) are not very highly correlated with the

indices of the related climate modes, but for convenience of reference, in the following sections we refer to the first seven leading modes as ENSO, global warming pattern, the PMM, AMO, PDO, AMM, and interannual AMO, respectively.

4. Tropical SST effects on Northern Hemisphere TC genesis and occurrence frequency

4.1 Effects on basin-wide TC genesis and occurrence frequency

As discussed in the introduction, tropical SSTs exert strong influences on TCGF. Next, we will quantify the combined effects of the leading tropical SST modes on basin-wide TCGF in individual basins via a multiple linear regression analysis. Because TC data are more reliable after the advent of the satellite era, the regression analysis is applied to the most recent 50 years, i.e., 1969–2018 (1977–2018 for the NIO; see section 2.1 for a discussion on NIO TC data). The multiple linear regression analysis also allows us to quantify the relative importance of different tropical SST modes in TCGF over different basins.

Black curves in Fig. 2 show the temporal evolution of annual TCGFs in the best-track data during 1951–2018 over the four basins of the Northern Hemisphere. In the NIO, TCGF varies substantially on interannual timescales (the coefficient of variation is 0.35), and in the other three basins, TCGF exhibits strong variations on both interannual and decadal timescales. The TCGF reconstructed from the multiple linear regression analysis well reproduces the observations in the latter three basins, with the correlation coefficients around 0.77, 0.73 and 0.75 for the NA, NEP and NWP during 1969–2018 (or 59%, 53% and 56% in terms of explained variance; Figs. 2a–c), respectively. We note that if we assume the roles of the seven leading modes do not change with time (discussed in section 4.3), the dotted red curves for the period before 1969 indicate that some TCs may be missing in the pre-satellite era in these three basins, which is consistent with previous studies using various distinct approaches (e.g., Chang and Guo 2007; Vecchi and Knutson 2008,

2011; Mei et al. 2019). A quantitative assessment of the "missed" TCs based on the statistical reconstruction using tropical SST modes will be explored in the near future and presented in a separate manuscript. In the NIO, however, the reconstruction does not perform well in capturing the year-to-year variations in observed TCGF (Fig. 2d). The lack of skill over the NIO suggests a rather modest role of tropical SSTs in modulating TCGF over this basin and echoes the findings of previous studies (e.g., Camargo et al. 2007; Zhao et al. 2009; Camp et al. 2015; Murakami et al. 2017). From now on, we will focus our analysis on the three basins of the North Atlantic and North Pacific.

Figure 3a shows the regression coefficients and the statistical significance for NA, NEP and NWP. The AMO, ENSO, the AMM, and global warming pattern (including SST warming in the NA) are important for NA TCGF; the order of these four modes reflects their relative contributions (from high to low) to the interannual-to-decadal variability in NA TCGF (figure not shown). Specifically, a positive AMO, a negative ENSO, a positive AMM, and global warming pattern of the past five decades favor NA TC genesis.

We have reconstructed the SST pattern conducive to NA TC genesis using the spatial patterns of the seven leading SST modes (M1–M7) as follows:

$$\mathrm{SST}_{\mathrm{reconstruction}} = [(T-1)\sigma^2_{\mathrm{TCGF}}]^{-1}\widetilde{\mathbf{W}}_{1:7}(\widetilde{\mathbf{V}}'_{1:7}\widetilde{\mathbf{V}}_{1:7})\mathbf{b}\,, \qquad \text{Eq. (2)}$$

where T is the number of years during 1969–2018 (i.e., 50), σ^2_{TCGF} is the variance of observed NA TCGF during this period, $\widetilde{\mathbf{W}}_{1:7}$ is a matrix representing the spatial patterns of M1–M7 (Figs. 1a,c,e,g,i,k,m), $\widetilde{\mathbf{V}}_{1:7}$ is a matrix representing the corresponding PCs (i.e., the gray bars in Figs. 1b,d,f,h,j,l,n), and $\mathbf{b}$ is a column vector of the regression coefficients of PC1–PC7 (i.e., the values shown in Fig. 3a). Equation (2) applies to research addressing similar issues, and details on how it is derived are provided in Appendix A. Figure 4a displays the reconstructed SST pattern favorable

301 for NA TC genesis. It is evident that SST warming in the tropical NA and cooling in the equatorial
302 eastern Pacific tend to promote TC genesis in the NA, consistent with previous studies (e.g., Kossin
303 and Vimont 2007; Mei et al. 2014; Patricola et al. 2014). This reconstructed anomalous SST pattern
304 is nearly identical to the spatial map obtained from the linear regression of global SSTs onto
305 observed NA TCGF (Fig. 4b), indicating that the SST pattern favorable for NA TC genesis can be
306 represented by several SST modes.

307 For the NEP TCGF, the dominant modes are ENSO and the AMO, with El Niño and a
308 negative AMO producing more TCs (Fig. 3a). The signs of the regression coefficients show that
309 the effects of these modes on TC genesis are opposite between the NA and NEP, in line with
310 previous studies suggesting that TCGF in these two basins to some extent varies oppositely (Wang
311 and Lee 2009; Collins 2010; Caron et al. 2015). The spatial pattern of SST anomalies reconstructed
312 using the seven SST modes and multiple linear regression coefficients indicates that SST warming
313 in the tropical eastern Pacific (particularly north of the equator) and cooling in the tropical Atlantic
314 favor TC genesis in the NEP (Fig. 4c). As in the NA, this reconstructed SST pattern is consistent
315 with the SST pattern obtained from the linear regression of global SSTs on observed NEP TCGF
316 (Fig. 4d).

317 TCGF in the NWP is controlled by modes in association with the PMM, the interannual
318 component of the AMO, and the global warming pattern (primarily the SST changes in the Indian
319 and Atlantic Oceans) (Fig. 3a). Regression coefficients show that SST cooling in the tropical
320 Indian Ocean and tropical NA and warming in the tropical central North Pacific encourage TC
321 genesis in the NWP. This can be clearly seen in the pattern of SST anomalies reconstructed using
322 the leading SST modes (Fig. 4e) and from the linear regression of global SSTs against NWP TCGF
323 (Fig. 4f). These results are in line with previous studies emphasizing the importance of SSTs in all

three basins of the Northern Hemisphere in influencing NWP TCGF (e.g., Zhan et al. 2011; Mei et al. 2015; Yu et al. 2016; Zhang et al. 2016; Zhan et al. 2019).

In short, tropical SST variability strongly modulates the year-to-year variations in TCGF over the NA, NEP and NWP, but has no significant effect on those over the NIO. The SST modes that dominate TCGF differ among basins and may have opposite effects on TCGF of the NA, NEP and NWP. For all the three basins, a combination of the SST modes weighted by the coefficients obtained from the multiple linear regression of TCGF on the PCs of these modes well reproduces the pattern of SST anomalies that favors TC genesis. It is worth noting that TCGF in the NA and NEP is modulated by both local and remote SSTs, whereas TCGF in the NWP is only affected by remote SSTs.

We further repeated the above analyses on basin-wide TC occurrence frequency for the NA, NEP and NWP. The results show that tropical SST variations are more skillful in capturing the variability in occurrence frequency than the variability in genesis frequency, and account for around 61%, 67% and 69% of the variance in occurrence frequency during 1969–2018 in these three basins, respectively (figure not shown). The modes dominating occurrence frequency are also slightly different from those controlling genesis frequency (Fig. 3b). For the NA, the AMM does not significantly affect occurrence frequency despite its importance in modulating genesis frequency. For the NEP, the global warming pattern emerges as one important factor for variations in occurrence frequency, in addition to the factors affecting genesis frequency. For the NWP, the canonical ENSO stands out as one of the dominant contributors to occurrence frequency although it has minor effect on basin-wide genesis frequency.

4.2 Effects on the large-scale environment and local TC genesis and occurrence frequency

346 It has long been recognized that tropical SSTs cause the large-scale atmospheric
347 environment to vary, and that changes in large-scale dynamic and thermodynamic environmental
348 variables (e.g., 850-hPa relative vorticity and the magnitude of vertical wind shear) influence TC
349 genesis (Gray 1968; Emanuel and Nolan 2004; Fu et al. 2012; Peng et al. 2012). In this section,
350 we examine the individual effects of the seven SST modes on the large-scale atmospheric
351 condition and thereby on local and basin-wide TC genesis and occurrence frequency in the NA,
352 NEP and NWP during 1969–2018 via a linear regression analysis. The large-scale environmental
353 condition is represented by the GPI and its four components defined in section 2.2 based on the
354 JRA-55 Reanalysis dataset. To determine the contribution of one component (e.g., vertical wind
355 shear) to the changes in the GPI (in response to the SST modes), we recalculated the GPI using
356 the original, year-to-year varying values for that component but the climatology of 1969–2018 for
357 the other three components, following Camargo et al. (2007). This procedure was repeated for all
358 the four components of the GPI. As a result, positive anomalies in the subplots for the four
359 components of the GPI shown in Fig. 5 all indicate positive effects of the components on GPI,
360 which are produced by increased potential intensity, decreased mid-level saturation deficit,
361 decreased vertical wind shear, and increased low-level vorticity, respectively. It is worth noting
362 that the sum of the contributions of individual components quantified here is close but not equal
363 to the changes in GPI, because of the nonlinearity of the GPI formula, as discussed in Camargo et
364 al. (2007). Using the NCEP/NCAR Reanalysis 1 dataset produces very similar results regarding
365 the responses of the large-scale atmospheric environment to various tropical SST modes (Fig. S2),
366 demonstrating the robustness of the results.
367 In response to a positive-phase M1, genesis potential increases in the majority of the NEP
368 and the southeastern NWP but decreases in the western tropical NA (particularly over the

Caribbean Sea) and between 20°N and 40°N in the NWP (Fig. 5a). The reduction in GPI in the tropical NA is caused primarily by increased vertical wind shear and saturation deficit, and tends to suppress TC genesis and development in this region (Fig. 6a). The increased genesis potential in the NEP is due mainly to reduced wind shear and increased potential intensity (Fig. 5a), and favors TC activity in this basin (Figs. 6a,b). These contribute in part to the observation that TC counts in the NA and NEP vary oppositely (Table 1 and Fig. S3; e.g., Wang and Lee 2009; Collins et al. 2010). In the NWP, the increase in GPI in the southeastern portion is attributed to an increase in low-level vorticity and a decrease in wind shear, whereas the decrease in GPI in the northwestern portion is dominated by an increase in saturation deficit (Fig. 5a). This dipole pattern of GPI changes leads to out-of-phase changes in TCGF in the two sub-basin regions, but a rather modest change in basin-wide TC counts (Fig. 6a). Because TCs forming in the southeastern portion of the basin stay over the warm water for a relatively longer period of time and prefer recurving tracks, enhanced TC genesis in this area increases TC occurrence frequency over the entire basin except near the coastal regions around China (Figs. 6a,b). These results are in line with previous studies regarding the effects of the canonical ENSO on NWP TC activity (e.g., Wang and Chan 2002; Li 2012). The ENSO-induced changes in genesis potential over different basins shown here are also consistent with those described in Camargo et al. (2007) despite differences in the formulation of the GPI.

A positive phase of M2 tends to increase genesis potential over the tropical NA and the subtropical and mid-latitude NWP and to decrease genesis potential in the subtropical NA (Fig. 5b). In the tropical NA, reduced wind shear and enhanced potential intensity are the main contributors to the increase in GPI. The resultant increase in TCGF over the Caribbean Sea and eastern tropical NA produces a basin-wide increase in TC occurrence frequency (Figs. 6c,d). In

392 the subtropical NA, particularly off the East Coast of the southeastern U.S., the decrease in GPI is
393 primarily attributed to decreased potential intensity and increased saturation deficit, and suppresses
394 TC genesis in the region (Fig. 6c). This region, however, still experiences above-normal TC
395 occurrence frequency because of promoted TC genesis in the tropical NA (Figs. 6c,d). In the
396 subtropical and mid-latitude NWP, the increase in genesis potential is mainly caused by increased
397 potential intensity and decreased saturation deficit, promoting local TC genesis. We note that the
398 regressed map of TC genesis on PC2 shows that TC genesis is significantly suppressed in the
399 southeastern NWP during the positive phase of M2 (Fig. 6c). This is not suggestive based on the
400 GPI anomalies, and may be attributed to the decreased low-level vorticity and increased wind shear
401 in this region (Fig. 5b). The suppressed TC genesis in the southeastern NWP results in lower-than-
402 normal TC occurrence frequency over the entire NWP (Fig. 6d), which is in accord with previous
403 studies showing that the Indian or Atlantic Ocean warming may discourage NWP TC genesis
404 (Zhan et al. 2011; Yu et al. 2016). In the NEP, the effect of strengthened wind shear counteracts
405 that of reduced saturation deficit (Fig. 5b), leading to neutral large-scale condition and no
406 significant changes in TC genesis (Fig. 6c). In the subtropical and mid-latitude NEP, increased
407 saturation deficit reduces genesis potential (Fig. 5b), which, however, has no effect on TC genesis
408 because TCs rarely form in this region in the present climate (Fig. 6c).

409 During a positive phase of M3, genesis potential is significantly increased over the tropical
410 North Pacific, except in the coastal regions (Fig. 5c). In the NWP, both low-level vorticity and
411 wind shear contribute to the increase in GPI, leading to increased TC genesis and occurrence
412 frequency over the entire basin (Figs. 6e,f). In the NEP, reduced wind shear dominates the increase
413 in genesis potential, and meanwhile, increased saturation deficit and reduced low-level vorticity
414 decrease genesis potential near the coastal areas of central America. As a result, a dipole pattern

of TC genesis anomaly emerges in the NEP, with more (less) TCs forming west (east) of 115°W (Fig. 6e); the basin-wide TCGF, however, does not change. The dipole of TC genesis changes also produces a dipole pattern of TC occurrence frequency in the NEP (Fig. 6f; Murakami et al. 2017). Over the NA, M3 has no statistically significant effect on the tropical large-scale environment and TC genesis and occurrence frequency.

M4, in association with the AMO, affects genesis potential primarily in the tropical NA, yielding favorable environments during its positive phase (Fig. 5d). This increase in GPI is caused by reduced wind shear and increased potential intensity, resulting in more TCs in the tropical NA and above-normal TC occurrence frequency over the entire basin (Figs. 6g,h). In the NEP, increased vertical wind shear appears to suppress TC genesis and occurrence frequency over the majority of the basin during the positive phase of M4, despite little changes in GPI (Fig. 5d). The weak response of GPI to M4 in the NEP shown here and to M2 in the southeastern NWP discussed above indicate that the formula of GPI in use is more sensitive to thermodynamic properties and not sensitive enough to dynamical factors of vertical wind shear and low-level vorticity in some regions, which is likely due to the complex interplay between the individual terms (Menkes et al. 2012). In the NWP, while the subtropics experiences an increase in genesis potential, changes in GPI over the tropics are small, leading to sporadic changes in local TCGF and no significant changes in basin-wide TC genesis and occurrence frequency (Figs. 6g,h).

Genesis potential and TC activity over most of the Northern Hemisphere, except the NEP, are insensitive to M5 (Figs. 5e, 6i,j). In the NEP, M5 produces significant changes in GPI through changes in vertical wind shear and low-level vorticity, and during its positive phase leads to discernible but insignificant increases in TCGF and significant increases in TC occurrence frequency over this basin (Figs. 6i,j).

438 During the positive phase of M6, when the tropical NA and South Atlantic respectively
439 experience anomalous warming and cooling, genesis potential is significantly increased in the
440 tropical NA, particularly in the eastern portion (Fig. 5f). This increase in genesis potential can be
441 attributed to reduced wind shear and increased potential intensity, and results in significantly
442 increased TC genesis in this region, accompanied by an insignificant increase in TC occurrence
443 frequency (Figs. 6k,l). The responses in other Northern Hemisphere basins are not statistically
444 significant.

445 M7 is associated with the interannual component of the AMO. During its positive phase,
446 genesis potential is increased in the tropical NA but decreased in the tropical NEP (Fig. 5g). The
447 increase in the tropical NA is contributed by both decreased wind shear and increased potential
448 intensity, leading to above-normal TC genesis in this basin (Fig. 6m). In the NEP, the decreased
449 genesis potential is caused by increased saturation deficit and decreased potential intensity (Fig.
450 5g), which in turn can be linked to the cold anomaly north of 20°N in the NEP (Fig. 1m). As a
451 result, the NEP experiences an inactive TC season in terms of both genesis and occurrence
452 frequency (Figs. 6m,n). Thus, this mode also contributes to the observation of out-of-phase
453 changes in seasonal TC counts over the NA and NEP (Fig. S3). In addition, in response to the
454 positive phase of M7, genesis potential tends to decrease over the NWP, particularly in the
455 southeastern portion of the basin (Fig. 5g). The decrease in genesis potential is primarily due to
456 increased vertical wind shear and decreased low-level vorticity (Fig. 5g), and leads to suppressed
457 TC genesis and occurrence in the NWP (Fig. 3 and Figs. 6m,n). The effect of M7 on NWP TC
458 activity may be achieved through the effect of tropical NA SST anomalies on Indian Ocean SSTs
459 and/or on the Walker circulation (e.g., Yu et al. 2016; Zhang et al. 2018). A numerical study fully

460 exploring the effects of tropical NA SSTs with a high-resolution AGCM will shed light on this
461 interesting topic.

462 **4.3 Interdecadal modulations of tropical SST effects on basin-wide TCGF**

463 Over different periods of time, the modes that dominate the variations of TCGF over a
464 basin may vary. In this section, we examine how the dominant modes identified in the previous
465 subsections for the period 1969–2018 change with time. Specifically, for each basin we apply the
466 multiple linear regression analysis to various 30-year periods with the starting year sliding from
467 1969 to 1989 (i.e., 1969–1998, 1970–1999, …, 1989–2018). For each of these 30-year periods, we
468 obtain the regression coefficients of the leading SST modes and the correlation skill of the
469 reconstructed TCGF.

470 Figure 7a shows the regression coefficients for the PCs of M1–M7 as a function of the
471 starting year of the regression period obtained from the regression analysis of NA TCGF. Both M1
472 (associated with the canonical ENSO) and M4 (associated with the AMO) exert strong influences
473 on NA TC genesis, with cooling in the central-to-eastern equatorial Pacific and warming in the
474 tropical NA promoting TC genesis, independent of the study period. The regression coefficients
475 of these two modes become larger with time, and this can be attributed to both increased variance
476 in TCGF and decreased variance in the two PCs (figure not shown). The global warming pattern
477 (i.e., M2), which is shown to significantly affect NA TCGF during 1969–2018 in section 4.1, plays
478 a significant role only in the 30-year periods starting before the mid-1970s. Additional multiple
479 linear regression analyses in which PC2 is divided into interannual and decadal components
480 suggest that such a significance is due primarily to the decadal component of this mode. The AMM
481 (i.e., M6) modulates NA TC counts mainly after the mid-1980s.

The correlation coefficient between the reconstructed and observed TCGF varies modestly with time, and is greater than 0.8 over most of the time (solid red curve in Fig. 7b), indicating the strong and stable control by tropical SSTs. We have also performed a similar sliding-window multiple linear regression analysis but using the six climate indices that correspond to the seven leading tropical SST modes: Niño-3.4, global-mean SST, the PMM, AMO, PDO and AMM. The reconstructed TCGF (solid black curve in Fig. 7b) is also highly correlated with the observations, but the skill is lower than the reconstruction based on the leading modes of the tropical SST variations.

The modes related to the canonical ENSO and AMO (i.e., M1, M4 and M7) dominate TCGF variations in the NEP, with both El Niño and negative AMO favoring more TCs, as discussed in sections 4.1 and 4.2. Because both modes affect NA TCGF in an opposite way compared to their effect on NEP TCGF, a significant correlation exists in seasonal TC counts between these two basins, particularly between the NA and western NEP (i.e., west of 112°W; Fig. S3; Collins et al. 2010). The importance of ENSO in modulating NEP TCGF increases with time and becomes significant after the mid-1970s (Fig. 7c), strengthening the anticorrelation in TCGF correspondingly (Fig. S3). As in the NA, the regression coefficients of M1 and M4 increase with time, which is also due to both increased variance in TCGF and decreased variance in PCs (figure not shown). What is different from the NA is that the mode related to the interannual AMO (i.e., M7) also modulates NEP TC counts over most of the time (cf. Figs. 7a,c).

TCGF reconstructed based on the SST modes captures 50–75% of the variations in NEP TCGF over a 30-year period, with the correlation skill improving with time during 1969–2018 (Fig. 7d). The increase in correlation skill is especially prominent around the mid-1970s, and suggests strengthened modulations of NEP TC genesis by tropical SST variations, particularly the

505 continuously increased importance of ENSO discussed above. The rising contribution of ENSO is
506 further confirmed via multiple linear regression analyses with the PC of one SST mode excluded
507 as well as a sliding-window correlation analysis of PC1 and NEP TCGF (figure not shown). The
508 empirical model built on the six climate indices is less skillful and accounts for only 25–50% of
509 the variance in observed TCGF; it, however, also shows increased skill after the mid-1970s (Fig.
510 7d).

511 As shown in Fig. 7e, TCGF in the NWP is high during the positive phase of M3 (i.e., the
512 PMM) throughout the entire study period. The negative phases of M7 (i.e., the interannual AMO)
513 and of M2 (i.e., global warming) also encourage NWP TC genesis, with the former important
514 before the mid-1980s and the latter effective after the mid-1980s. The TCGF reconstructed using
515 the seven SST modes is highly correlated with the observations ($r > 0.8$), and the correlation skill
516 is stable during 1969–2018 (solid red curve in Fig. 7f). The statistical model based on the six
517 climate indices exhibits a comparable skill, but underperforms prior to 1975 (solid black curve in
518 Fig. 7f).

519 In all the three basins, excluding the modes that do not significantly affect TCGF (Fig. 3a)
520 slightly reduces the correlation skill of the reconstructions based on multiple linear regression (cf.
521 solid and dashed red curves in Figs. 7b,d,f). We have also repeated all the above analyses but
522 removed the trends in both TCGF and PCs of the SST modes before performing multiple
523 regression analysis, and obtained very similar results (figure not shown), which suggests that
524 secular trends play a minor role. In all three basins, the modulation of basin-wide TC occurrence
525 frequency by tropical SST variations exhibits similar interdecadal changes as the modulation of
526 basin-wide TCGF, and is consistently stronger than the latter (Fig. S4).

527 **5. Summary and conclusions**

528 This study has investigated the influence of warm-season tropical sea surface temperature
529 (SST) variations on Northern Hemisphere tropical cyclone (TC) genesis frequency (TCGF) using
530 observed SSTs and TC best-track data. Specifically, we first extracted the leading modes of
531 tropical SST variability during the TC peak season (June–November) via an empirical orthogonal
532 function (EOF) analysis, and then quantified the individual and combined effects of these SST
533 modes on TCGF in each Northern Hemisphere ocean basin by means of multiple linear regression
534 analysis. We further interpreted the SST effects by analyzing the response of a genesis potential
535 index (GPI) and its components to the identified SST modes. Potential interdecadal modulations
536 of the tropical SST effects on TCGF are also examined. The main results are summarized as
537 follows.

538 The first seven modes of tropical SST variability modulate TC activity in one or more of
539 the basins in the Northern Hemisphere, and together account for around 80% of the variance in
540 tropical SSTs. These modes are related to the canonical El Niño–Southern Oscillation (ENSO),
541 global warming, Pacific Meridional Mode (PMM), Atlantic Multidecadal Oscillation (AMO),
542 Pacific Decadal Oscillation (PDO), Atlantic Meridional Mode (AMM) and interannual component
543 of AMO, respectively (Fig. 1).

544 Multiple linear regression analyses show that these SST modes together capture 59%, 53%
545 and 56% of the variance in TCGF during 1969–2018 over the North Atlantic (NA), Northeast
546 Pacific (NEP) and Northwest Pacific (NWP), respectively (Figs. 2a–c); the captured variance in
547 basin-wide TC occurrence frequency is 61%, 67% and 69% in these three basins, respectively.
548 This demonstrates the strong control of TC activity in the NA and North Pacific by tropical SST
549 forcing. A linear combination of the leading SST modes weighted by the coefficients obtained
550 from the multiple linear regression of TCGF on the PCs of these modes well reproduces the pattern

551 of SST anomalies that favors TC genesis (Fig. 4). The SST patterns suggest that TC counts in the
552 NA and NEP are governed by both local and remote SSTs, whereas TC counts in the NWP are
553 affected solely by remote SSTs. The effect of these SST modes on TC activity in the North Indian
554 Ocean is weak (Fig. 2d), in line with previous studies based on simulations with dynamical models
555 and analyses of GPI.

556 In the NA, basin-wide TCGF is modulated by the AMO, canonical ENSO, global warming
557 and AMM: La Niña, the positive AMO and AMM, and global warming pattern favor more TCs
558 (Fig. 3a). The first three of these four SST modes also significantly affect basin-wide occurrence
559 frequency (Fig. 3b). In the NEP, the modes dominating basin-wide TCGF are in association with
560 the canonical ENSO and AMO, with more TCs occurring during El Niño years and the negative
561 phase of the AMO. The basin-wide TC occurrence frequency is also significantly influenced by
562 the mode associated with the PDO, in addition to those tied to ENSO and the AMO. In the NWP,
563 basin-wide TCGF is promoted during the positive phase of the mode associated with the PMM
564 and the negative phase of the modes associated with global warming and the interannual
565 component of the AMO (Fig. 3a). These three modes together with the mode linked to the
566 canonical ENSO determine basin-wide occurrence frequency in the NWP (Fig. 3b).

567 Because TC genesis in the NWP and that in the NEP are favored under a positive PMM
568 and a negative AMO (primarily on the interannual timescales), TC counts of these two basins have
569 components that vary synchronously (r = 0.44; Table 1). On the other hand, TCGF in the NA is
570 significantly negatively correlated with that in the North Pacific (r = -0.35), particularly in the
571 NEP after the 1980s (Fig. S3). The negative correlation between the NA and NEP TCGF is
572 attributed to the fact that a La Niña state and a positive AMO favor TC genesis in the NA but
573 discourage genesis in the NEP. As a result, the variance of the combined TCGF of these three

574 basins (i.e., 58.0; Table 1) is smaller than the sum of TCGF variances of individual basins (i.e.,
575 19.5, 24.7 and 19.2 for the NA, NEP and NWP, respectively; Table 1).[1]

576 To understand how these SST modes affect basin-wide TC genesis and occurrence
577 frequency, we further examined their effects on the large-scale atmospheric environment and on
578 local TC genesis and occurrence frequency via linear regression analysis (Figs. 5 and 6). The large-
579 scale environment is represented by the GPI and its four components (including potential intensity,
580 mid-level saturation deficit, vertical wind shear and low-level vorticity). The results suggest that a
581 specific SST mode may affect TC genesis in different areas via different mechanisms. In general,
582 TCGF in the NA is modulated primarily via changes in potential intensity and vertical wind shear,
583 in line with Bruyère et al. (2012) and Mei et al. (2019). In the NEP, vertical wind shear emerges
584 as the dominant factor for variations in TCGF, with potential intensity and mid-tropospheric
585 saturation deficit making additional contributions. In the NWP, changes in low-level vorticity and
586 vertical wind shear control TCGF in the southeastern quadrant of the basin, whereas mid-level
587 saturation deficit is more important in the northwestern quadrant. In addition, the results echo
588 previous studies regarding the opposite effects of the canonical ENSO on TC genesis in different
589 parts of the NWP: El Niño tends to increase TC genesis in the southeast quadrant via increased
590 low-level vorticity and reduced vertical wind shear, and suppress TC genesis in the northwestern
591 quadrant via increased mid-level saturation deficit and decreased potential intensity.

[1] To further explain this statement, let X be the NA TCGF, Y be the NEP TCGF, and Z be the NWP TCGF. The variance of X+Y+Z can be written as $\mathrm{Var}(X+Y+Z) = \mathrm{Var}(X) + \mathrm{Var}(Y) + \mathrm{Var}(Z) + 2\mathrm{Cov}(X,Y) + 2\mathrm{Cov}(X,Z) + 2\mathrm{Cov}(Y,Z) = \mathrm{Var}(X) + \mathrm{Var}(Y) + \mathrm{Var}(Z) + 2\sqrt{\mathrm{Var}(X)\mathrm{Var}(Y)}r(X,Y) + 2\sqrt{\mathrm{Var}(X)\mathrm{Var}(Z)}r(X,Z) + 2\sqrt{\mathrm{Var}(Y)\mathrm{Var}(Z)}r(Y,Z)$, where $r(a, b)$ represents the correlation coefficient between a and b. According to Table 1, $r(X,Y) = -0.31$ and $r(X,Z) = -0.28$, which lead to a negative value of $2\sqrt{\mathrm{Var}(X)\mathrm{Var}(Y)}r(X,Y) + 2\sqrt{\mathrm{Var}(X)\mathrm{Var}(Z)}r(X,Z) + 2\sqrt{\mathrm{Var}(Y)\mathrm{Var}(Z)}r(Y,Z)$, despite $r(Y,Z) = 0.44$. This produces $\mathrm{Var}(X+Y+Z) < \mathrm{Var}(X) + \mathrm{Var}(Y) + \mathrm{Var}(Z)$.

To identify potential changes with time in the impacts of tropical SST forcing on basin-wide TCGF in the NA, NEP and NWP, we performed multiple linear regression analysis for various 30-year periods with the starting year sliding from 1969 to 1989. It is found that the contribution of tropical SSTs to the variations in TCGF is quite stable and around 70% for a 30-year period in both the NA and NWP (Figs. 7b,f). In contrast, tropical SSTs become more effective in modulating TC counts in the NEP, particularly after the mid-1970s (Fig. 7d). This can be attributed to the increased contribution of ENSO (Fig. 7c), and explains the strengthened anticorrelation in TC counts between the NA and NEP (Fig. S3).

Our work shows that warm-season tropical SSTs contribute to more than half of the year-to-year variations in TC counts over the North Atlantic and Pacific basins during 1969–2018. We note that TC activity has been linked to tropical SST modes in pre-seasons (e.g., Zhan et al. 2019), a connection that needs to be investigated in future studies. Other contributing factors may include atmospheric and SST forcing from the extratropics (e.g., the North Atlantic Oscillation, Rossby wave breaking and subpolar gyre SST temperature), and forcing from the tropical land (e.g., western Sahel rainfall and dust concentration) (e.g., Landsea et al. 1999; Elsner et al. 2000; Jagger et al. 2001; Fink et al. 2010; Kossin et al. 2010; Smith et al. 2010; Dunstone et al. 2011; Caron et al. 2015; Lim et al. 2016; Patricola et al. 2018; Zhang and Wang 2019). In addition, internal variability associated with the instability of the tropical atmosphere also contributes (Chen and Lin 2011; Wu et al. 2012; Done et al. 2014; Mei et al. 2014, 2015, 2019). A thorough and accurate quantification of these factors remains challenging and may be achieved via large-ensemble simulations with high-resolution coupled models.

Acknowledgements

This work was supported by the Department of Homeland Security's Coastal Resilience Center of Excellence, a startup fund from the University of North Carolina at Chapel Hill, and National Science Foundation Grant AGS-2047721 (W.M.). We thank Dr. Chris Landsea, the editor and an anonymous reviewer for their comments, which greatly helped improve the manuscript.

Appendix A

Let $\mathbf{Y}_0$ be an $N \times T$ data matrix (e.g., tropical SSTs in this study; N is the number of grid points in space, T is the length of the data in time domain, and $N > T$), and $\mathbf{Y} = \mathbf{Y}_0(\mathbf{I}_T - T^{-1}\mathbf{J}_T)$ be the centered matrix of $\mathbf{Y}_0$, where $\mathbf{I}_T$ is the $T \times T$ identity matrix and $\mathbf{J}_T$ is a $T \times T$ matrix of ones. Consider the singular value decomposition (SVD) of $\mathbf{Y}$: $\mathbf{Y} = \mathbf{UDV}' = \mathbf{WV}' = \sum_{j=1}^{T} d_j u_j v_j'$, where $\mathbf{D} = \mathrm{Diag}(d_1, \ldots, d_T)$ is an $N \times T$ rectangular diagonal matrix with the singular values in non-increasing order, and $\mathbf{U}'\mathbf{U} = \mathbf{I}_N$ and $\mathbf{V}'\mathbf{V} = \mathbf{I}_T$. Assume that $\mathbf{1}'\mathbf{X} = 0$, where $\mathbf{1}$ is a $T \times 1$ vector of ones and $\mathbf{X}$ is a $T \times 1$ vector (e.g., TCGF after removing the long-term mean in this study). Regressing $\mathbf{Y}$ on $\mathbf{X}$: $\mathbf{Y} = \beta\mathbf{X}' + \boldsymbol{\epsilon}$ gives the least squares estimator of the regression coefficient β:

$$\hat{\beta} = (\mathbf{X}'\mathbf{X})^{-1}\mathbf{YX}\,, \tag{A1}$$

Given the SVD of $\mathbf{Y}$ and considering only its first k modes, $\hat{\beta}$ is approximated by

$$\tilde{\beta} = (\mathbf{X}'\mathbf{X})^{-1}\mathbf{W}_{1:k}(\mathbf{V}_{1:k}'\mathbf{X})\,, \tag{A2}$$

where $\mathbf{W}_{1:k}$ and $\mathbf{V}_{1:k}$ are the first k columns of $\mathbf{W}$ and $\mathbf{V}$, respectively (e.g., only the first seven modes of tropical SST variability are considered in this study).

Note that $\mathbf{V}_{1:k}'\mathbf{X}$ is the coefficient of the projection of $\mathbf{X}$ onto $\mathbf{V}_{1:k}$, and the unbiased variance of $\mathbf{X}$ is $\sigma_{\mathbf{X}}^2 = (T-1)^{-1}\mathbf{X}'\mathbf{X}$. If $\mathbf{1}'\mathbf{V}_{1:k} = (0,0,\ldots,0)_{1\times k}$, then the variance of v_j is $(T-1)^{-1}$, $j =$

637 $1, \ldots, k$. Define the normalized principal components $\widetilde{\mathbf{V}}_{1:k} = (\tilde{v}_1, \ldots, \tilde{v}_k) = \sqrt{T-1}\mathbf{V}_{1:k}$. Under the

638 assumption that $\mathbf{1}'\mathbf{X} = 0$ and $\mathbf{1}'\mathbf{V}_{1:k} = (0,0, \ldots,0)_{1\times k}$,

639 $$\tilde{\beta} = \frac{1}{(T-1)^{1/2}\sigma_{\mathbf{X}}^2}\widetilde{\mathbf{U}}_{1:k}\left(\frac{1}{(T-1)}\widetilde{\mathbf{V}}'_{1:k}\mathbf{X}\right), \quad \text{(A3)}$$

640 Let $\mathbf{b} = (T-1)^{-1}\mathbf{V}'_{1:k}\mathbf{X}$, which can be viewed as the coefficients of the projection of $\mathbf{X}$ onto $\widetilde{\mathbf{V}}_{1:k}$

641 if $\widetilde{\mathbf{V}}'_{1:k}\widetilde{\mathbf{V}}_{1:k} = (T-1)\mathbf{I}_k$. In practice, a correction term is added to adjust the biases due to numerical

642 approximations so that

643 $$\tilde{\beta} = \frac{1}{\sigma_{\mathbf{X}}^2}\left[(T-1)^{-1/2}\mathbf{W}_{1:k}\right]\left(\frac{1}{(T-1)}\widetilde{\mathbf{V}}'_{1:k}\widetilde{\mathbf{V}}_{1:k}\right)\mathbf{b} = [(T-1)\sigma_{\mathbf{X}}^2]^{-1}\widetilde{\mathbf{W}}_{1:k}(\widetilde{\mathbf{V}}'_{1:k}\widetilde{\mathbf{V}}_{1:k})\mathbf{b}\,. \quad \text{(A4)}$$

644 where $\widetilde{\mathbf{W}}_{1:k} = (T-1)^{-1/2}\mathbf{W}_{1:k}$ (e.g., the rescaled spatial patterns of the first seven modes of

645 tropical SST variability shown in Figs. 1a,c,e,g,i,k,m). Such an adjustment is made by noting that

646 the least squares estimator of θ in the regression model $\mathbf{X} = \widetilde{\mathbf{V}}_{1:k}\theta + \mathbf{e}$ is $\mathbf{b} = \left(\widetilde{\mathbf{V}}'_{1:k}\widetilde{\mathbf{V}}_{1:k}\right)^{-1}\widetilde{\mathbf{V}}'_{1:k}\mathbf{X}$.

647

648

649 **References**

650 Aiyyer, A. R., and C. Thorncroft, 2006: Climatology of vertical wind shear over the tropical
651 Atlantic. *J. Climate*, **19**, 2969–2983, https://doi.org/10.1175/JCLI3685.1.

652 Amaya, D. J., 2019: The Pacific Meridional Mode and ENSO: a Review. *Curr. Clim. Change Rep.*,
653 **5**, 296–307, https://doi.org/10.1007/s40641-019-00142-x.

654 Ashok, K., S. K. Behera, S. A. Rao, H. Weng, and T. Yamagata, 2007: El Niño Modoki and its
655 possible teleconnection. *J. Geophys. Res.*, **112**, C11007,
656 https://doi.org/10.1029/2006JC003798.

657 Barcikowska, M., F. Feser, W. Zhang, and W. Mei, 2017: Changes in intense tropical cyclone
658 activity for the western North Pacific during the last decades derived from a regional
659 climate model simulation. *Climate Dyn.*, **9–10**, 2931–2949,
660 https://doi.org/10.1007/s00382-016-3420-0.

661 Bruyère, C. L., G. J. Holland, and E. Towler, 2012: Investigating the use of a genesis potential
662 index for tropical cyclones in the North Atlantic basin. *J. Climate*, **25**, 8611–8626,
663 https://doi.org/10.1175/JCLI-D-11-00619.1.

664 Camargo, S. J., K. A. Emanuel, and A. H. Sobel, 2007: Use of a genesis potential index to diagnose
665 ENSO effects on tropical cyclone genesis. *J. Climate*, **20**, 4819–4834,
666 https://doi.org/10.1175/JCLI4282.1.

667 Camargo, S. J., A. W. Robertson, A. G. Barnston, and M. Ghil, 2008: Clustering of eastern North
668 Pacific tropical cyclone tracks: ENSO and MJO effects. *Geochem. Geophys. Geosys.*, **9**,
669 Q06V05, https://doi.org/10.1029/2007GC001861.

670 Camargo, S. J., A. H. Sobel, A. G. Barnston, and P. J. Klotzbach, 2010: The influence of natural
671 climate variability, and seasonal forecasts of tropical cyclone activity. *Global Perspectives*
672 *on Tropical Cyclones, from Science to Mitigation,* 2nd ed., J. C. L. Chan and J. D. Kepert,
673 Eds., 325–362.

674 Camp, J., M. Roberts, C. MacLachlan, E. Wallace, L. Hermanson, A. Brookshaw, A. Arribas, and
675 A. A. Scaife, 2015: Seasonal forecasting of tropical storms using the Met Office GloSea5
676 seasonal forecast system. *Quart. J. Roy. Meteor. Soc.*, **141**, 2206–2219,
677 https://doi.org/10.1002/qj.2516.

678 Capotondi, A., and P. D. Sardeshmukh, 2015: Optimal precursors of different types of ENSO
679 events. *Geophys. Res. Lett.*, **42**, 9952–9960, https://doi.org/10.1002/2015GL066171.

680 Caron, L.-P., M. Boudreault, and S. J. Camargo, 2015: On the variability and predictability of
681 eastern North Pacific tropical cyclone activity. *J. Climate*, **28**, 9678–9696,
682 https://doi.org/10.1175/JCLI-D-15-0377.1.

683 Chan, J. C. L., 1985: Tropical cyclone activity in the Northwest Pacific in relation to the El
684 Niño/Southern Oscillation phenomenon. *Mon. Wea. Rev.*, **113**, 599–606, doi:
685 10.1175/1520-0493(1985)113<0599:TCAITN>2.0.CO;2.

686 Chang, E. K. M., and Y. Guo, 2007: Is the number of North Atlantic tropical cyclones significantly
687 underestimated prior to the availability of satellite observations? *Geophys. Res. Lett.*, **34**,
688 L14801, https://doi.org/10.1029/2007GL030169.

689 Chen, G., and C. Y. Tam, 2010: Different impacts of two kinds of Pacific Ocean warming on
690 tropical cyclone frequency over the western North Pacific. *Geophys. Res. Lett.*, **37**, L01803,
691 https://doi.org/10.1029/2009GL041708.

692 Chen, J.-H., and S.-J. Lin, 2011: The remarkable predictability of inter-annual variability of
693 Atlantic hurricanes during the past decade. *Geophys. Res. Lett.*, **38**, L11804,
694 https://doi.org/10.1029/2011GL047629.

695 Chen, X., and J. M. Wallace, 2016: Orthogonal PDO and ENSO indices. *J. Climate*, **29**, 3883–
696 3892, https://doi.org/10.1175/JCLI-D-15-0684.1.

697 Chiang, J. C. H., and D. J. Vimont, 2004: Analogous Pacific and Atlantic meridional modes of
698 tropical atmosphere–ocean variability. *J. Climate*, **17**, 4143–4158,
699 https://doi.org/10.1175/JCLI4953.1.

700 Choi, Y., K. J. Ha, C. H. Ho, and C. E. Chung, 2015: Interdecadal change in typhoon genesis
701 condition over the western North Pacific. *Climate Dyn.*, **45**, 3243–3255,
702 https://doi.org/10.1007/s00382-015-2536-y.

703 Chu, J.-H., C. R. Sampson, A. S. Levine, and E. Fukada, 2002: The joint typhoon warning center
704 tropical cyclone best-tracks, 1945–2000. Naval Research Laboratory Rep. NRL/MR/7540-
705 02-16, 22 pp.

706 Clark, J. D., and P.-S. Chu, 2002: Interannual variation of tropical cyclone activity over the central
707 North Pacific. *J. Meteor. Soc. Japan*, **80**, 403–418, https://doi.org/10.2151/jmsj.80.403.

708 Collins, J. M., 2010: Contrasting high North-East Pacific tropical cyclone activity with low North
709 Atlantic activity. *Southeast. Geogr.*, **50**, 83–98, https://doi.org/10.1353/sgo.0.0069.

710 Collins, J. M., P. J. Klotzbach, R. N. Maue, D. R. Roache, E. S. Blake, C. H. Paxton, and C. A.
711 Mehta, 2016: The record-breaking 2015 hurricane season in the eastern North Pacific: An
712 analysis of environmental conditions. *Geophys. Res. Lett.*, **43**, 9217–9224,
713 https://doi.org/10.1002/2016GL070597.

714 Done, J. M., C. L. Bruyère, M. Ge, and A. Jaye, 2014: Internal variability of North Atlantic tropical
715 cyclones. *J. Geophys. Res. Atmos.*, **119**, 6506–6519,
716 https://doi.org/10.1002/2014JD021542.

717 Dong, L., and T. Zhou, 2014: The formation of the recent cooling in the eastern tropical Pacific
718 Ocean and the associated climate impacts: A competition of global warming, IPO, and
719 AMO. *J. Geophys. Res.*, **119**, 11272–11287, https://doi.org/10.1002/2013JD021395.

720 Du, Y., L. Yang, and S.-P. Xie, 2011: Tropical Indian Ocean influence on northwest Pacific
721 tropical cyclones in summer following strong El Niño. *J. Climate*, **24**, 315–322,
722 https://doi.org/10.1175/2010JCLI3890.1.

723 Dunstone, N. J., D. M. Smith, and R. Eade, 2011: Multi-year predictability of the tropical Atlantic
724 atmosphere driven by the high latitude North Atlantic Ocean. *Geophys. Res. Lett.*, **38**,
725 L14701, https://doi.org/10.1029/2011GL047949.

726 Elsner, J. B., and A. B. Kara, 1999: Hurricanes of the North Atlantic: Climate and society. Oxford
727 University Press, New York.

728 Elsner, J. B., K. Liu, and B. Kocher, 2000: Spatial variations in major U.S. hurricane activity:
729 Statistics and a physical mechanism. *J. Climate*, **13**, 2293–2305, doi: 10.1175/1520-
730 0442(2000)013<2293:SVIMUS>2.0.CO;2.

731 Emanuel, K. A., 2003: Tropical cyclones. *Annu. Rev. Earth Planet. Sci.*, **31**, 75–104,
732 https://doi.org/10.1146/annurev.earth.31.100901.141259.

733 Emanuel, K. A., 2010: Tropical cyclone activity downscaled from NOAA-CIRES reanalysis,
734 1908–1958. *J. Adv. Model. Earth Syst.*, **2**, https://doi.org/10.3894/JAMES.2010.2.1.

735 Emanuel, K. A., 2018: 100 years of progress in tropical cyclone research. *A Century of Progress*
736 *in Atmospheric and Related Sciences: Celebrating the American Meteorological Society*
737 *Centennial*, *Meteor. Monogr.*, 15.1–15.68, https://doi.org/10.1175/AMSMONOGRAPHS-
738 D-18-0016.1.

739 Emanuel, K. A., and D. S. Nolan, 2004: Tropical cyclone activity and the global climate system.
740 *26th Conf. on Hurricanes and Tropical Meteorology*, Miami, FL, Amer. Meteor. Soc.,
741 10A.2, http://ams.confex.com/ams/pdfpapers/75463.pdf.

742 Felton, C. S., B. Subrahmanyam, and V. S. N. Murty, 2013: ENSO modulated cyclogenesis over
743 the Bay of Bengal. *J. Climate*, **26**, 9806–9818, https://doi.org/10.1175/JCLI-D-13-
744 00134.1.

745 Fink, A. H., J. M. Schrage, and S. Kotthaus, 2010: On the potential causes of the nonstationary
746 correlations between West African precipitation and Atlantic hurricane activity. *J. Climate*,
747 **23**, 5437–5456, https://doi.org/10.1175/2010JCLI3356.1.

748 Fu, B., M. S. Peng, T. Li, and D. E. Stevens, 2012: Developing versus nondeveloping disturbances
749 for tropical cyclone formation. Part II: Western North Pacific. *Mon. Wea. Rev.*, **140**, 1067–
750 1080, https://doi.org/10.1175/2011MWR3618.1.

751 Gao, S., Z. Chen, and W. Zhang, 2018: Impacts of tropical North Atlantic SST on western North
752 Pacific landfalling tropical cyclones. *J. Climate*, **31**, 853–862,
753 https://doi.org/10.1175/JCLI-D-17-0325.1.

754 Goldenberg, S. B., and L. J. Shapiro, 1996: Physical mechanisms for the association of El Niño
755 and West African rainfall with Atlantic major hurricane activity. *J. Climate*, **9**, 1169–1187,
756 https://doi.org/10.1175/1520-0442(1996)009<1169:PMFTAO>2.0.CO;2.

757 Goldenberg, S. B., C. W. Landsea, A. M. Mestas-Nuñez, and W. M. Gray, 2001: The recent
758 increase in Atlantic hurricane activity: Causes and implications. *Science*, **293**, 474–479,
759 https://doi.org/10.1126/science.1060040.

760 Gray, W. M., 1968: Global view of the origin of tropical disturbances and storms. *Mon. Wea. Rev.*,
761 **96**, 669–700, https://doi.org/10.1175/1520-0493(1968)096<0669:GVOTOO>2.0.CO;2.

762 Gray, W. M., 1984: Atlantic seasonal hurricane frequency. Part I: El Niño and 30 mb quasi-
763 biennial oscillation influences. *Mon. Wea. Rev.*, **112**, 1649–1668,
764 https://doi.org/10.1175/1520-0493(1984)112,1649:ASHFPI.2.0.CO;2.

765 Ha, Y., Z. Zhong, X. Yang, and Y. Sun, 2015: Contribution of East Indian Ocean SSTA to western
766 North Pacific tropical cyclone activity under El Niño/La Niña conditions. *Int. J. Climatol.*,
767 **35**, 506–519, https://doi.org/10.1002/joc.3997.

768 Ham, Y.-G., J.-S. Kug, J.-Y. Park, and F.-F. Jin, 2013: Sea surface temperature in the north tropical
769 Atlantic as a trigger for El Niño/Southern Oscillation events. *Nat. Geosci.*, **6**, 112–116,
770 https://doi.org/10.1038/ngeo1686.

771 Huang, B., and Coauthors, 2017: Extended reconstructed sea surface temperature version 5
772 (ERSSTv5): Upgrades, validations, and intercomparisons. *J. Climate*, **30**, 8179–8205.

773 Huo, L., P. Guo, S. N. Hameed, and D. Jin, 2015: The role of tropical Atlantic SST anomalies in
774 modulating western North Pacific tropical cyclone genesis. *Geophys. Res. Lett.*, **42**, 2378–
775 2384, https://doi.org/10.1002/2015GL063184.

776 Irwin, R. P., and R. E. Davis, 1999: The relationship between the Southern Oscillation index and
777 tropical cyclone tracks in the eastern North Pacific. *Geophys. Res. Lett.*, **26**, 2251–2254,
778 https://doi.org/10.1029/1999GL900533.

779 Jagger, T. H., J. B. Elsner, and X. Niu, 2001: A dynamic probability model of hurricane winds in
780 coastal counties of the United States. *J. Appl. Meteor.*, **40,** 853–863, doi: 10.1175/1520-
781 0450(2001)040<0853:ADPMOH>2.0.CO;2.

782 Jiang, N., and C. Zhu, 2018: Asymmetric changes of ENSO diversity modulated by the cold tongue
783 mode under recent global warming. *Geophys. Res. Lett.* **45,** 12506–12513, doi:
784 10.1029/2018GL079494.

785 Jien, J. Y., W. A. Gough, and K. Butler, 2015: The influence of El Niño–Southern Oscillation on
786 tropical cyclone activity in the eastern North Pacific basin. *J. Climate*, **28**, 2459–2474,
787 https://doi.org/10.1175/JCLI-D-14-00248.1.

788 Ju, J. H., L. L. Chen, and C.Y. Li, 2004: The preliminary research of Pacific–Indian Ocean sea
789 surface temperature anomaly mode and the definition of its index. *Journal of Tropical*
790 *Meteorology*, **20**, 617–624.

791 Kalnay, E., and Coauthors, 1996: The NCEP/NCAR 40-Year Reanalysis Project. *Bull. Amer.*
792 *Meteor. Soc.*, **77**, 437–471.

793 Kao, H.-Y, and J.-Y. Yu, 2009: Contrasting eastern-Pacific and central-Pacific types of ENSO. *J.*
794 *Climate*, **22**, 615–632, https:// doi.org/10.1175/2008JCLI2309.1.

795 Kim, H.-M., P. J. Webster, and J. A. Curry, 2011: Modulation of North Pacific tropical cyclone
796 activity by three phases of ENSO. *J. Climate*, **24**, 1839–1849, https://doi.org/10.1175/
797 2010JCLI3939.1.

798 Klotzbach, P. J., 2011: The influence of El Niño–Southern Oscillation and the Atlantic
799 multidecadal oscillation on Caribbean tropical cyclone activity. *J. Climate*, **24**, 721–731,
800 https://doi.org/10.1175/2010JCLI3705.1.

801 Klotzbach, P. J., and E. S. Blake, 2013: North-central Pacific tropical cyclones: Impacts of El
802 Niño–Southern Oscillation and the Madden–Julian oscillation. *J. Climate*, **26**, 7720–7733,
803 https://doi.org/10.1175/JCLI-D-12-00809.1.

804 Knutson, T. R., J. J. Sirutis, S. T. Garner, G. A. Vecchi, and I. M. Held, 2008: Simulated reduction
805 in Atlantic hurricane frequency under twenty-first-century warming conditions. *Nat.*
806 *Geosci.*, **1**, 359–364, https://doi.org/10.1038/ngeo202.

807 Knutson, T. R., and Coauthors, 2010: Tropical cyclones and climate change. *Nat. Geosci.*, **3**, 157–
808 163, https://doi.org/10.1038/ngeo779.

809 Korty, R. L., S. J. Camargo, and J. Galewsky, 2012: Tropical cyclone genesis factors in simulations
810 of the Last Glacial Maximum. *J. Climate*, **25**, 4348–4365, https://doi.org/10.1175/JCLI-D-
811 11-00517.1.

812 Kossin, J. P., and D. J. Vimont, 2007: A more general framework for understanding Atlantic
813 hurricane variability and trends. *Bull. Amer. Meteor. Soc.*, **88**, 1767–1781,
814 https://doi.org/10.1175/BAMS-88-11-1767.

815 Kossin, J. P., S. J. Camargo, and M. Sitkowski, 2010: Climate modulation of North Atlantic
816 hurricane tracks. *J. Climate*, **23**, 3057–3076, https://doi.org/10.1175/2010JCLI3497.1.

817 Kobayashi, S., and Coauthors, 2015: The JRA-55 reanalysis: General specifications and basic
818 characteristics. *J. Meteor. Soc. Japan*, **93**, 5–48, https://doi.org/10.2151/jmsj.2015-001.

819 Kucharski, F., A. Bracco, J. H. Yoo, and F. Molteni, 2008: Atlantic forced component of the Indian
820 monsoon interannual variability. *Geophys. Res. Lett.*, **35**, L04706,
821 https://doi.org/10.1029/2007GL033037.

822 Landsea, C. W., R. A. Pielke, A. M. Mestas-Nuñez, and J. A. Knaff, 1999: Atlantic basin
823 hurricanes: Indices of climatic changes. *Climatic Change*, **42**, 89–129,
824 https://doi.org/10.1023/A:1005416332322.

825 Landsea, C. W., G. A. Vecchi, L. Bengtsson, and T. R. Knutson, 2010: Impact of duration
826 thresholds on Atlantic tropical cyclone counts. *J. Climate*, **23**, 2508–2519.

827 Landsea, C. W., and J. L. Franklin, 2013: Atlantic hurricane database uncertainty and presentation
828 of a new database format. *Mon. Wea. Rev.*, **141**, 3576–3592,
829 https://doi.org/10.1175/MWR-D-12-00254.1.

830 Larson, S. M., and B. P. Kirtman, 2014: The Pacific meridional mode as an ENSO precursor and
831 predictor in the North American multimodel ensemble. *J. Climate*, **27**, 7018–7032,
832 https://doi.org/10.1175/JCLI-D-14-00055.1.

833 Lau, N.-C., 1985: Modeling the seasonal dependence of the atmospheric response to observed El
834 Niños in 1962–76. *Mon. Wea. Rev.*, **113**, 1970–1996, https://doi.org/10.1175/1520-
835 0493(1985)113<1970:MTSDOT>2.0.CO;2.

836 Li, T., 2012: Synoptic and Climatic Aspects of Tropical Cyclogenesis in Western North Pacific in
837 Cyclones: Formation, Triggers, and Control. K. Oouchi and H. Fudevasu, Eds., Noval
838 Science Publishers, 61–94.

839 Lim, Y.-K., S. D. Schubert, O. Reale, A. M. Molod, M. J. Suarez, and B. M. Auer, 2016: Large-
840 scale controls on Atlantic tropical cyclone activity on seasonal time scales. *J. Climate*, **29**,
841 6727–6749.

842 Liu, C., W. Zhang, M. Stuecker, and F.-F. Jin, 2019: Pacific Meridional Mode-Western North
843 Pacific Tropical Cyclone Linkage Explained by Tropical Pacific Quasi-Decadal
844 Variability. *Geophys. Res. Lett.*, **46**, 13346–13354.

845 Liu, Y., P. Huang, and G. Chen, 2019: Impacts of the combined modes of the tropical Indo-Pacific
846 sea surface temperature anomalies on the tropical cyclone genesis over the western North
847 Pacific. *Int. J. Climatol.*, **39**, 2108–2119.

848 Mei, W., S.-P. Xie, and M. Zhao, 2014: Variability of tropical cyclone track density in the North
849 Atlantic: Observations and high-resolution simulations. *J. Climate*, **27**, 4797–4814,
850 https://doi.org/10.1175/JCLI-D-13-00587.1.

851 Mei, W., S.-P. Xie, M. Zhao, and Y. Wang, 2015: Forced and internal variability of tropical
852 cyclone track density in the western North Pacific. *J. Climate*, **28**, 143–167,
853 https://doi.org/10.1175/JCLI-D-14-00164.1.

854 Mei, W., Y. Kamae, S.-P. Xie, and K. Yoshida, 2019: Variability and Predictability of North
855 Atlantic Hurricane Frequency in a Large Ensemble of High-Resolution Atmospheric
856 Simulations. *J. Climate,* **32**, 3153–3167, https://doi.org/10.1175/JCLI-D-18-0554.1.

857 Menkes, C. E., M. Lengaigne, P. Marchesiello, N. C. Jourdain, E. M. Vincent, J. Lefevre, F.
858 Chauvin, and J.-F. Royer, 2012: Comparison of tropical cyclogenesis indices on seasonal
859 to interannual timescales. *Climate Dyn.*, **38**, 301–321.

860 Messié, M., and F. Chavez, 2011: Global modes of sea surface temperature variability in relation
861 to regional climate indices. *J. Climate*, **24**, 4314–4331,
862 https://doi.org/10.1175/2011JCLI3941.1.

863 Murakami, H., G. A. Vecchi, and S. Underwood, 2017: Increasing frequency of extremely severe
864 cyclonic storms over the Arabian Sea. *Nat. Climate Change*, **7**, 885–889,
865 https://doi.org/10.1038/s41558-017-0008-6.

866 Murakami, H., and Coauthors, 2017: Dominant role of subtropical Pacific warming in extreme
867 eastern Pacific hurricane seasons: 2015 and the future. *J. Climate*, **30**, 243–264,
868 https://doi.org/10.1175/JCLI-D-16-0424.1.

869 Nolan, D. S., and M. G. McGauley, 2012: Tropical cyclogenesis in wind shear: Climatological
870 relationships and physical processes. *Cyclones: Formation, Triggers, and Control*.
871 Kazuyoshi Oouchi and Hironori Fudeyasu, eds., Nova Science Publishers, Happauge, New
872 York, pp. 1–36.

873 North, G., T. Bell, R. Cahalan, and F. Moeng, 1982: Sampling errors in the estimation of Empirical
874 Orthogonal Functions. *Mon. Wea. Rev.*, **110**, 699–706.

875 Palmer, T. N., and D. A. Mansfeld, 1984: Response of two atmospheric general circulation models
876 to sea-surface temperature anomalies in the tropical East and West Pacific. *Nature*, **310**,
877 483–485, https://doi.org/10.1038/310483a0.

878 Patricola, C. M., R. Saravanan, and P. Chang, 2014: The impact of the El Niño–Southern
879 Oscillation and Atlantic meridional mode on seasonal Atlantic tropical cyclone activity. *J.*
880 *Climate*, **27**, 5311–5328, https://doi.org/10.1175/JCLI-D-13-00687.1.

881 Patricola, C. M., R. Saravanan, and P. Chang, 2018: The response of Atlantic tropical cyclones to
882 suppression of African easterly waves. *Geophys. Res. Lett.*, **45**, 471–479,
883 https://doi.org/10.1002/2017GL076081.

884 Peng, M. S., B. Fu, T. Li, and D. E. Stevens, 2012: Developing versus nondeveloping disturbances
885 for tropical cyclone formation. Part I: North Atlantic. *Mon. Wea. Rev.*, **140**, 1047–1066,
886 https://doi.org/10.1175/2011MWR3617.1.

887 Rayner, N. A., D. E. Parker, E. B. Horton, C. K. Folland, L. V. Alexander, D. P. Rowell, E. C.
888 Kent, and A. Kaplan, 2003: Global analyses of sea surface temperature, sea ice, and night
889 marine air temperature since the late nineteenth century. *J. Geophys. Res.*, **108**, 4407,
890 https://doi.org/10.1029/2002JD002670.

891 Ren, F., J. Liang, G. Wu, W. Dong, and X. Yang, 2011: Reliability analysis of climate change of
892 tropical cyclone activity over the western North Pacific. *J. Climate*, **24**, 5887–5898.

893 Schreck, C. J., K. R. Knapp, and J. P. Kossin, 2014: The Impact of Best Track Discrepancies on
894 Global Tropical Cyclone Climatologies using IBTrACS. *Mon. Wea. Rev.*, **142**, 3881–3899,
895 https://doi.org/10.1175/MWR-D-14-00021.1.

896 Singh, O. P., T. M. A. Khan, and M. S. Rahman, 2000: Changes in the frequency of tropical
897 cyclones over the North Indian Ocean. *Meteor. Atmos. Phys.*, **75**, 11–20.

898 Smith, D. M., R. Eade, N. J. Dunstone, D. Fereday, J. M. Murphy, H. Pohlmann, and A. A. Scaife,
899 2010: Skillful multi-year predictions of Atlantic hurricane frequency. *Nat. Geosci.*, **3**, 846–
900 849, https://doi.org/10.1038/ngeo1004.

901 Tang, B. H., and J. D. Neelin, 2004: ENSO influence on Atlantic hurricanes via tropospheric
902 warming. *Geophys. Res. Lett.,* **31**, L24204, https://doi.org/10.1029/2004GL021072.

903 Tang, B. H., and K. Emanuel, 2012: A ventilation index for tropical cyclones. *Bull. Amer. Meteor.*
904 *Soc.*, **93**, 1901–1912, https://doi.org/10.1175/BAMS-D-11-00165.1.

905 Tao, L., L. Wu, Y. Wang, and J. Yang, 2012: Influence of tropical Indian Ocean warming and
906 ENSO on tropical cyclone activity over the western North Pacific. *J. Meteor. Soc. Japan*,
907 **90**, 127–144, https://doi.org/10.2151/jmsj.2012-107.

908 Tokinaga, H., S.-P. Xie, A. Timmermann, S. McGregor, T. Ogata, H. Kubota, and Y. M. Okumura,
909 2012: Regional patterns of tropical Indo-Pacific climate change: Evidence of the Walker
910 circulation weakening. *J. Climate*, **25**, 1689–1710.

911 Tory, K. J., and W. M. Frank, 2010: Tropical cyclone formation. *Global Perspectives on Tropical*
912 *Cyclones*, J. C. L. Chan and J. D. Kepert, Ed., World Scientific, 55–91.

913 Vecchi, G. A., and T. R. Knutson, 2008: On Estimates of Historical North Atlantic Topical
914 Cyclone Activity. *J. Climate*, **21**(14), 3580–3600.

915 Vecchi, G. A., and T. R. Knutson, 2011: Estimating annual numbers of Atlantic hurricanes missing
916 from the HURDAT database (1878–1965) using ship track density. *J. Climate*, **24**, 1736–
917 1746, https://doi.org/10.1175/2010JCLI3810.1.

918 Vecchi, G. A., M. Zhao, H. Wang, G. Villarini, A. Rosati, A. Kumar, I. M. Held, and R. Gudgel,
919 2011: Statistical-dynamical predictions of seasonal North Atlantic hurricane activity. *Mon.*
920 *Wea. Rev.*, **139**, 1070–1082, https://doi.org/10.1175/2010MWR3499.1.

921 Villarini, G., G. A. Vecchi, T. R. Knutson, and J. A. Smith, 2011: Is the Recorded Increase in Short
922 Duration North Atlantic Tropical Storms Spurious? *J. Geophys. Res.*, **116**, D10114.

923 Vimont, D. J., and J. P. Kossin, 2007: The Atlantic meridional mode and hurricane activity.
924 *Geophys. Res. Lett.*, **34**, L07709, https://doi.org/10.1029/2007GL029683.

925 Wang, B., and J. C. L. Chan, 2002: How strong ENSO events affect tropical storm activity over
926 the western North Pacific. *J. Climate*, **15**, 1643–1658.

927 Wang, C., 2019: Three-ocean interactions and climate variability: A review and perspective.
928 *Climate Dyn.*, **53**, 5119–5136, https://doi.org/10.1007/s00382-019-04930-x.

929 Wang, C., and S.-K. Lee, 2009: Co-variability of tropical cyclones in the North Atlantic and the
930 eastern North Pacific. *Geophys. Res. Lett.*, **36**, L24702,
931 https://doi.org/10.1029/2009GL041469.

932 Watterson, I. G., J. L. Evans, and B. F. Ryan, 1995: Seasonal and interannual variability of tropical
933 cyclogenesis: Diagnostics from large-scale fields. *J. Climate*, **8,** 3052–3066.

934 Whitney, L. D., and J. Hobgood, 1997: The relationship between sea surface temperature and
935 maximum intensities of tropical cyclones in the eastern North Pacific. *J. Climate*, **10**, 2921–
936 2930.

937 Wood, K. M., P. J. Klotzbach, J. M. Collins, and C. J. Schreck, 2019: The record-setting 2018
938 eastern North Pacific hurricane season. *Geophys. Res. Lett.*, **46**, 10,072–10,081.
939 https://doi.org/10.1029/2019gl083657.

940 Wu, C.-C., R. Zhan, Y. Lu, and Y. Wang, 2012: Internal variability of the dynamically downscaled
941 tropical cyclone activity over the western North Pacific by the IPRC regional atmospheric
942 model. *J. Climate*, **25**, 2104–2122, https://doi.org/10.1175/JCLI-D-11-00143.1.

943 Wu, L., H. Zhang, J.-M. Chen, and T. Feng, 2018: Impact of two types of El Niño on tropical
944 cyclones over the western North Pacific: Sensitivity to location and intensity of Pacific
945 warming. *J. Climate*, **31**, 1725–1742, https://doi.org/10.1175/JCLI-D-17-0298.1.

946 Wu, R., X. Cao, and Y. Yang, 2020: Interdecadal change in the relationship of the western North
947 Pacific tropical cyclogenesis frequency to tropical Indian and North Atlantic Ocean SST

in early 1990s. *J. Geophys. Res. Atmos.*, **125**, e2019JD031493. https://doi.org/10.1029/2019JD031493.

Xie, L., T. Yan, and L. J. Pietrafesa, 2005: The effect of Atlantic sea surface temperature dipole mode on hurricanes: Implications for the 2004 Atlantic hurricane season. *Geophys. Res. Lett.,* **32,** L03701, https://doi.org/10.1029/2004GL021702.

Xie, S.-P., and J. A. Carton, 2004: Tropical Atlantic variability: Patterns, mechanisms, and impacts. *Earth's Climate: The Ocean–Atmosphere Interaction*, *Geophys. Monogr*., Vol. 147, Amer. Geophys. Union, 121–142.

Xie, S.-P., K. Hu, J. Hafner, Y. Du, G. Huang, and H. Tokinaga, 2009: Indian Ocean capacitor effect on Indo-western Pacific climate during the summer following El Niño. *J. Climate*, **22**, 730–747.

Xie, S.-P., Y. Kosaka, Y. Du, K. Hu, J. Chowdary, and G. Huang, 2016: Indo-western Pacific Ocean capacitor and coherent climate anomalies in post-ENSO summer: A review. *Adv. Atmos. Sci.*, **33**, 411–432, https://doi.org/10.1007/s00376-015-5192-6.

Yeh, S.-W., J.-S. Kug, B. Dewitte, M.-H. Kwon, B. P. Kirtman, and F.-F. Jin, 2009: El Niño in a changing climate. *Nature*, **461**, 511–514, https://doi.org/10.1038/nature08316.

Yu, J.-Y., Y. Zou, S. T. Kim, and T. Lee, 2012: The changing impact of El Niño on US winter temperatures. *Geophys. Res. Lett.*, **39**, L15702, https://doi.org/10.1029/2012GL052483.

Yu, J., T. Li, Z. Tan, and Z. Zhu, 2016: Effects of tropical North Atlantic SST on tropical cyclone genesis in the western North Pacific. *Climate Dyn.*, **46**, 865–877, https://doi.org/10.1007/s00382-015-2618-x.

969 Zhan, R., Y. Wang, and X. Lei, 2011: Contributions of ENSO and east Indian Ocean SSTA to the
970 interannual variability of northwest Pacific tropical cyclone frequency. *J. Climate*, **24**, 509–
971 521, https://doi.org/10.1175/2010JCLI3808.1.

972 Zhan, R., Y. Wang, and J. Zhao, 2019: Contributions of SST anomalies in the Indo-Pacific Ocean
973 to the interannual variability of tropical cyclone genesis frequency over the Western North
974 Pacific. *J. Climate*, **32**, 3357–3372, https ://doi.org/10.1175/JCLI-D-18-0439.1.

975 Zhang, G., and Z. Wang, 2015: Interannual variability of tropical cyclone activity and regional
976 Hadley circulation over the northeastern Pacific. *Geophys. Res. Lett.*, **42**, 2473–2481,
977 https://doi.org/10.1002/2015GL063318.

978 Zhang, G., and Z. Wang, 2019: North Atlantic Rossby wave breaking during the hurricane season:
979 Association with tropical and extratropical variability. *J. Climate*, **32**, 3777–3801,
980 https://doi.org/10.1175/JCLI-D-18-0299.1.

981 Zhang, W., G. A. Vecchi, H. Murakami, G. Villarini, and L. Jia, 2016: The Pacific meridional
982 mode and the occurrence of tropical cyclones in the western North Pacific. *J. Climate*, **29**,
983 381–398, https://doi.org/10.1175/JCLI-D-15-0282.1.

984 Zhang, W., G. A. Vecchi, H. Murakami, G. Villarini, T. Delworth, X. Yang, and L. Jia, 2018:
985 Dominant role of Atlantic multidecadal oscillation in the recent decadal changes in western
986 North Pacific tropical cyclone activity. *Geophys. Res. Lett.*, **45**, 354–362,
987 https://doi.org/10.1002/2017GL076397.

988 Zhao, H., and C. Wang, 2019: On the relationship between ENSO and tropical cyclones in the
989 western North Pacific during the boreal summer. *Climate Dyn.*, **52**, 275–288,
990 https://doi.org/ 10.1007/s00382-018-4136-0.

991 Zhao, M., I. M. Held, S. J. Lin, and G. A. Vecchi, 2009: Simulations of global hurricane
992 climatology, interannual variability, and response to global warming using a 50-km
993 resolution GCM. *J. Climate*, **22**, 6653–6678, https://doi.org/10.1175/2009JCLI3049.1.

994 Zehr, R., 1992: Tropical cyclogenesis in the western North Pacific. NOAA Tech. Rep. NESDIS
995 61, U. S. Department of Commerce, Washington, DC, 181 pp.

996

997

998 **List of Tables**

999 Table 1: Correlation coefficients between TCGF of different basins/regions and variance of TCGF
1000 in different basins/regions during 1969–2018. Values significant at the 0.05 level are bold.

1001

1002 **List of Figures**

1003 Fig. 1. (a,c,e,g,i,k,m) The boreal warm-season (i.e., June–November) SST anomalies regressed
1004 against the principal components (PCs) of the first seven leading modes (M1–M7) of the tropical
1005 SSTs during 1951–2018. Only values significant at the 0.05 level are shown (shading).
1006 (b,d,f,h,j,l,n) The normalized PCs (grey bars) of M1–M7. Also shown are normalized climate
1007 indices: Niño-3 index (blue) and the Indian Ocean Dipole (IOD) index (red) in (b), global-mean
1008 SST (blue) in (d), the Pacific Meridional Mode (PMM) index (blue) and El Niño Modoki index
1009 (EMI; red) in (f), the detrended Atlantic Multidecadal Oscillation (AMO) index (blue) in (h), the
1010 Pacific Decadal Oscillation (PDO) index of April–July (blue) in (j), the Atlantic Meridional Mode
1011 (AMM) index (blue) in (l), and the 8-year high-pass-filtered AMO index (blue) in (n).

1012 Fig. 2. The observed (black) and reconstructed (red) TC genesis frequency (TCGF) during 1951–
1013 2018 for the (a) NA, (b) NEP, (c) NWP and (d) NIO. The reconstruction is based on the multiple
1014 linear regression of TCGF and PCs of the seven leading SST modes (grey bars in Fig. 1) during
1015 1969–2018 (1977–2018 for the NIO).

1016 Fig. 3. The coefficients for the PCs of the seven leading SST modes from the multiple linear
1017 regression analyses of (a) basin-wide TC genesis and (b) occurrence frequency during 1969–2018
1018 in the NA (black), NEP (red) and NWP (blue). For the NWP, dark green circles, diamonds and
1019 stars show results from the best track datasets produced by the CMA, JMA and JTWC,

1020 respectively. The filled bars and symbols indicate that the regression coefficients are significant at
1021 the 0.05 level.
1022 Fig. 4. (a,c,e) The pattern of SST anomalies (shading; unit: °C per TC) reconstructed using Eq. (2)
1023 for the NA (a), NEP (c) and NWP (e). Black dots show the climatology of TC genesis location
1024 during 1969–2018. (b,d,f) The regressed boreal warm-season SST anomalies (unit: °C per TC)
1025 against observed TCGF during 1969–2018 for the NA (b), NEP (d) and NWP (f). Black (grey)
1026 dots denote areas with regression coefficients significant at the 0.05 (0.1) level.
1027 Fig. 5. The regressed anomalies of GPI and its four components (i.e., potential intensity, mid-level
1028 saturation deficit, vertical wind shear and low-level vorticity) against the PC of (a) M1, (b) M2,
1029 (c) M3, (d) M4, (e) M5, (f) M6 and (g) M7 during 1969–2018. Black (grey) dots denote areas with
1030 regression coefficients significant at the 0.05 (0.1) level.
1031 Fig. 6. The regressed anomalies of TC genesis frequency (a,c,e,g,i,k,m) and occurrence frequency
1032 (b,d,f,h,j,l,n; unit: days) against the PC of M1 (a,b), M2 (c,d), M3 (e,f), M4 (g,h), M5 (i,j), M6
1033 (k,l) and M7 (m,n) during 1969–2018. Black (grey) dots denote areas with regression coefficients
1034 significant at the 0.05 (0.1) level.
1035 Fig. 7. (a,c,e) The coefficients for the PCs of M1–M7 from the multiple linear regression analysis
1036 of TCGF in the NA (a), NEP (c) and NWP (e) during various 30-year periods with the starting
1037 year sliding from 1969 to 1989 (i.e., 1969–1998, 1970–1999, …, 1989–2018). Black (grey) dots
1038 indicate that the regression coefficients are significant at the 0.05 (0.1) level. (b,d,f) The correlation
1039 skill of the TCGF reconstructed from the multiple linear regression using the PCs of M1–M7 (solid
1040 red) and using six climate indices (solid black) for various 30-year period with the starting year
1041 sliding from 1969 to 1989 (i.e., 1969–1998, 1970–1999, …, 1989–2018). The six climate indices
1042 in use include Niño-3.4, global-mean SST, indices of the PMM, AMO, PDO and AMM. Dashed

1043 red curves show the correlation skill of the TCGF reconstructed using only PCs of the modes
1044 dominant in the basin (i.e., M1, M2, M4 and M6 for the NA; M1, M4 and M7 for the NEP; M2,
1045 M3 and M7 for the NWP). Thin dashed black (grey) horizontal line represents the threshold for a
1046 correlation coefficient significant at the 0.05 (0.1) level.
1047
1048
1049
1050
1051

Tables

Table 1: Correlation coefficients (*r*) between TCGF of different basins/regions and variance of TCGF (Var(TCGF)) in different basins/regions during 1969–2018. Values significant at the 0.05 level are bold.

		NA	**NEP**	**NWP**	**NA+NEP**	**NA+NWP**	**NEP+NWP**	**NA+NEP+NWP**
r	**NA**		**-0.31**	-0.28			**-0.35**	0.21
	NEP			**0.44**		0.11		**0.73**
	NWP				0.17			**0.70**
Var(TCGF)		19.5	24.7	19.2	30.5	27.8	63.0	58.0

1061 **Figures**

1062

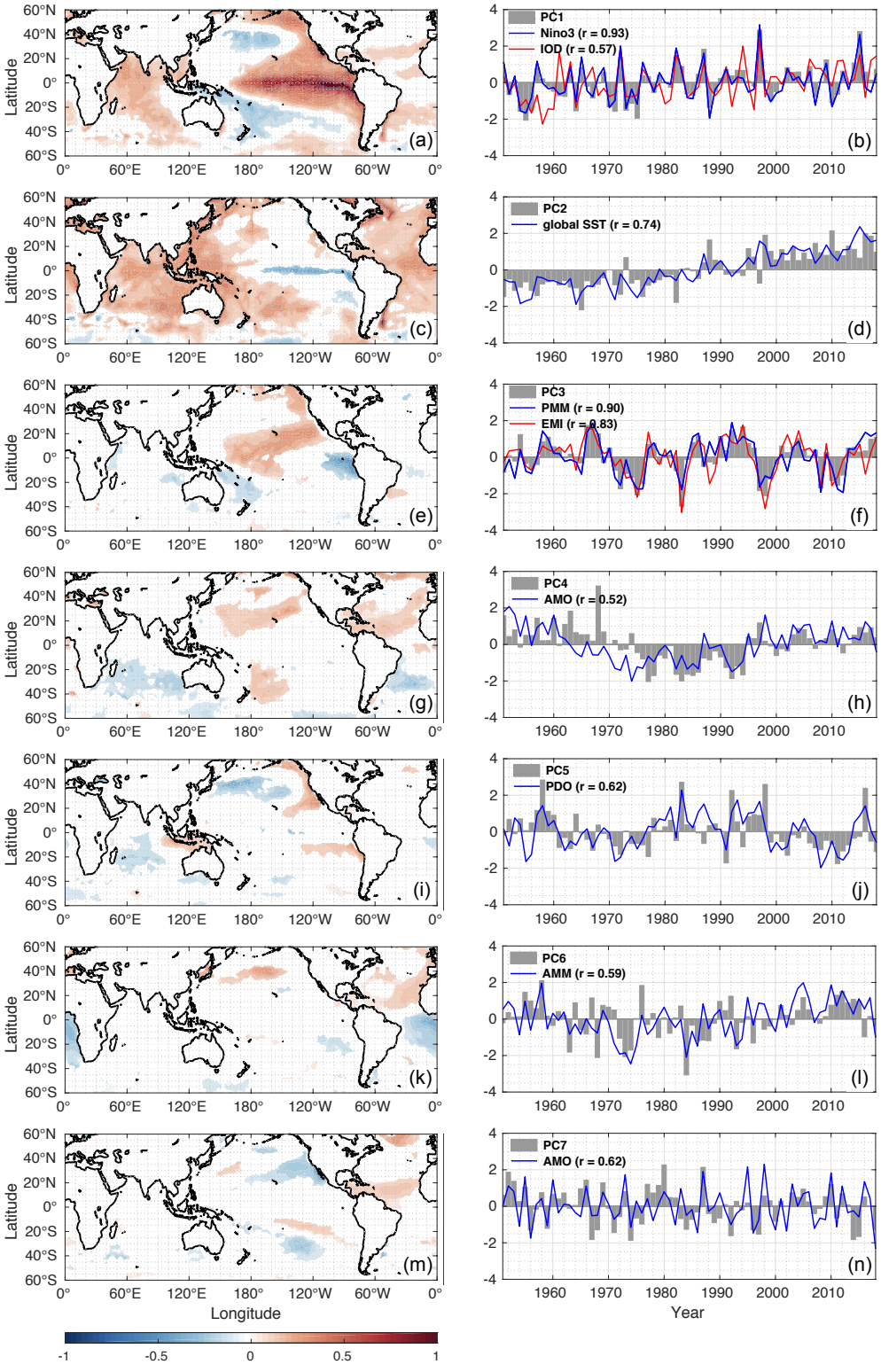

1063

Fig. 1. (a,c,e,g,i,k,m) The boreal warm-season (i.e., June–November) SST anomalies regressed against the principal components (PCs) of the first seven leading modes (M1–M7) of the tropical SSTs during 1951–2018. Only values significant at the 0.05 level are shown (shading). (b,d,f,h,j,l,n) The normalized PCs (grey bars) of M1–M7. Also shown are normalized climate indices: Niño-3 index (blue) and the Indian Ocean Dipole (IOD) index (red) in (b), global-mean SST (blue) in (d), the Pacific Meridional Mode (PMM) index (blue) and El Niño Modoki index (EMI; red) in (f), the detrended Atlantic Multidecadal Oscillation (AMO) index (blue) in (h), the Pacific Decadal Oscillation (PDO) index of April–July (blue) in (j), the Atlantic Meridional Mode (AMM) index (blue) in (l), and the 8-year high-pass-filtered AMO index (blue) in (n).

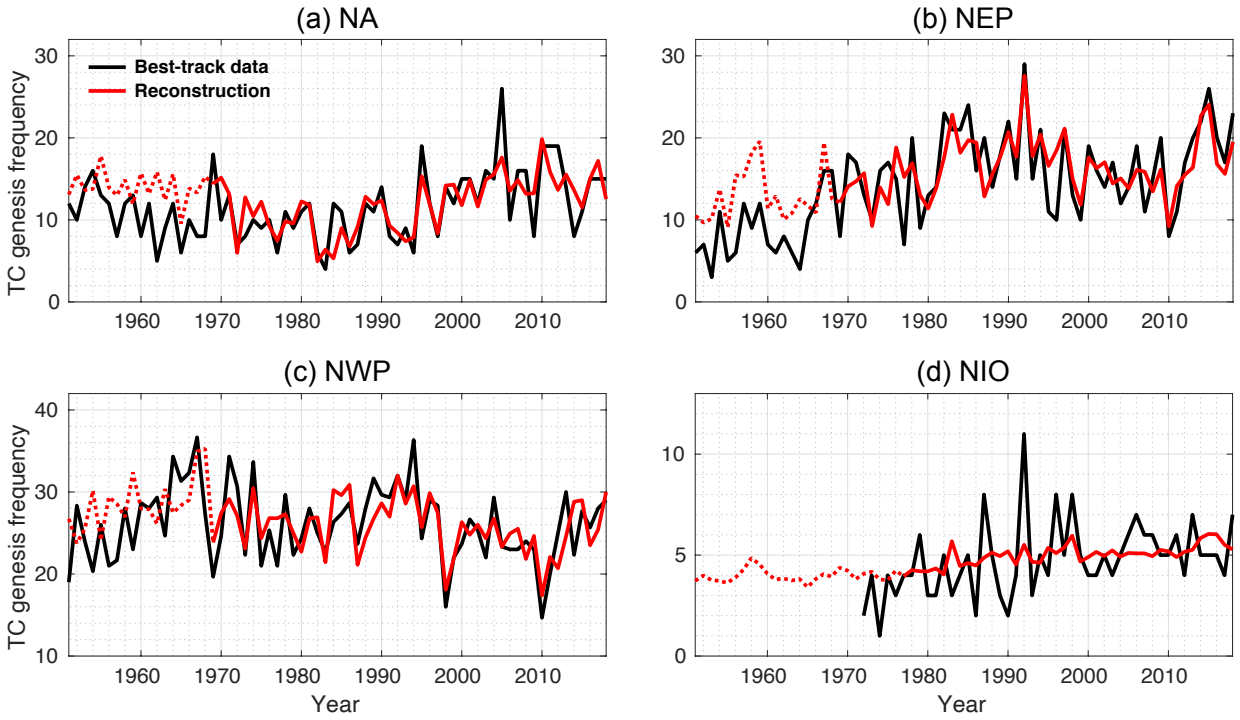

Fig. 2. The observed (black) and reconstructed (red) TC genesis frequency (TCGF) during 1951–2018 for the (a) NA, (b) NEP, (c) NWP and (d) NIO. The reconstruction is based on the multiple linear regression of TCGF and PCs of the seven leading SST modes (grey bars in Fig. 1) during 1969–2018 (1977–2018 for the NIO).

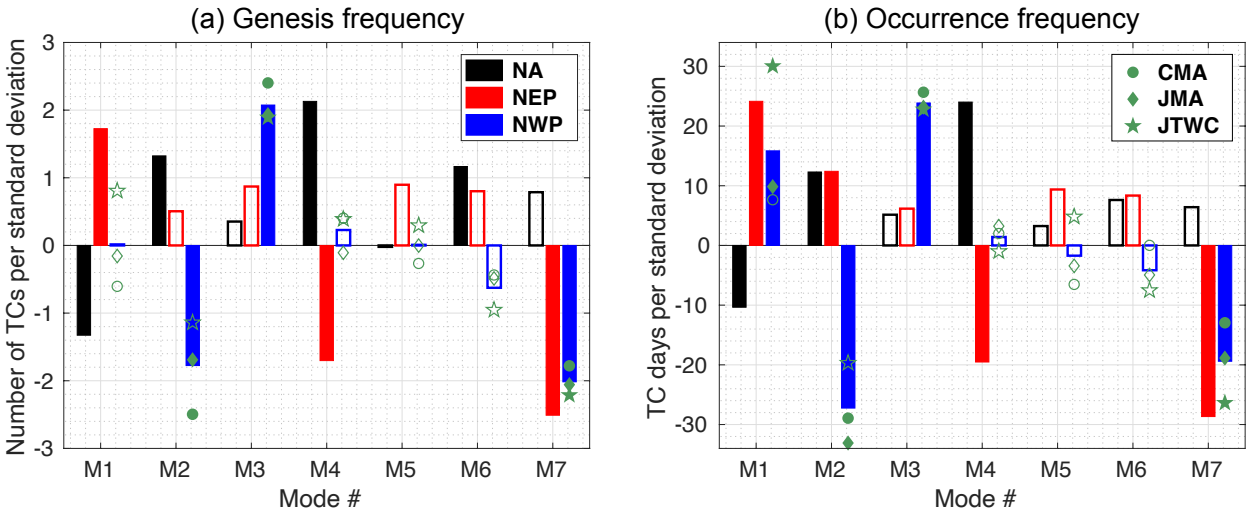

Fig. 3. The coefficients for the PCs of the seven leading SST modes from the multiple linear regression analyses of (a) basin-wide TC genesis and (b) occurrence frequency during 1969–2018 in the NA (black), NEP (red) and NWP (blue). For the NWP, dark green circles, diamonds and stars show results from the best track datasets produced by the CMA, JMA and JTWC, respectively. The filled bars and symbols indicate that the regression coefficients are significant at the 0.05 level.

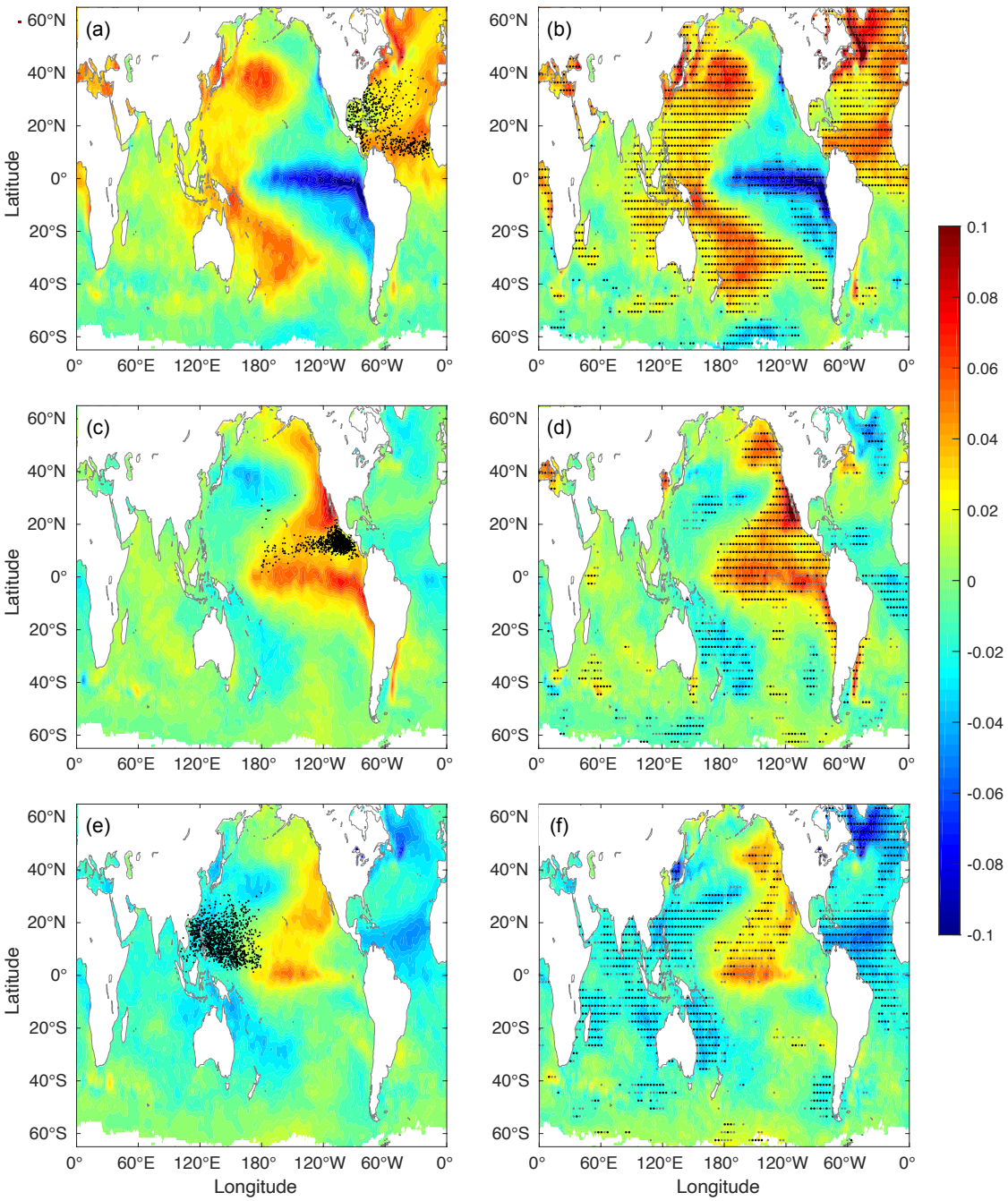

Fig. 4. (a,c,e) The pattern of SST anomalies (shading; unit: °C per TC) reconstructed using Eq. (2) for the NA (a), NEP (c) and NWP (e). Black dots show the climatology of TC genesis location during 1969–2018. (b,d,f) The regressed boreal warm-season SST anomalies (unit: °C per TC) against observed TCGF during 1969–2018 for the NA (b), NEP (d) and NWP (f). Black (grey) dots denote areas with regression coefficients significant at the 0.05 (0.1) level.

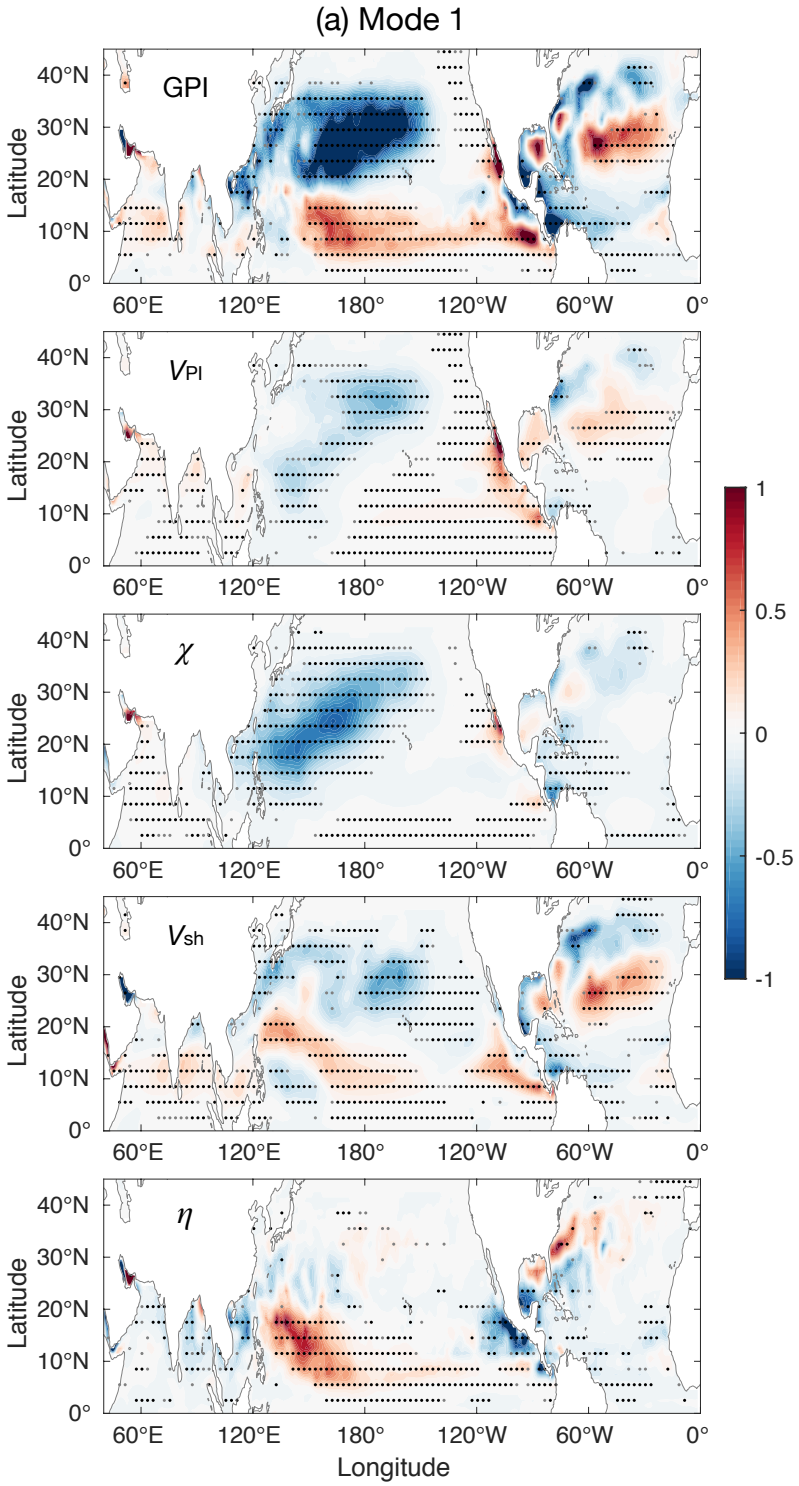

Fig. 5. The regressed anomalies of GPI and its four components (i.e., potential intensity, mid-level saturation deficit, vertical wind shear and low-level vorticity) against the PC of (a) M1, (b) M2,

1107 (c) M3, (d) M4, (e) M5, (f) M6 and (g) M7 during 1969–2018. Black (grey) dots denote areas with

1108 regression coefficients significant at the 0.05 (0.1) level.

1109

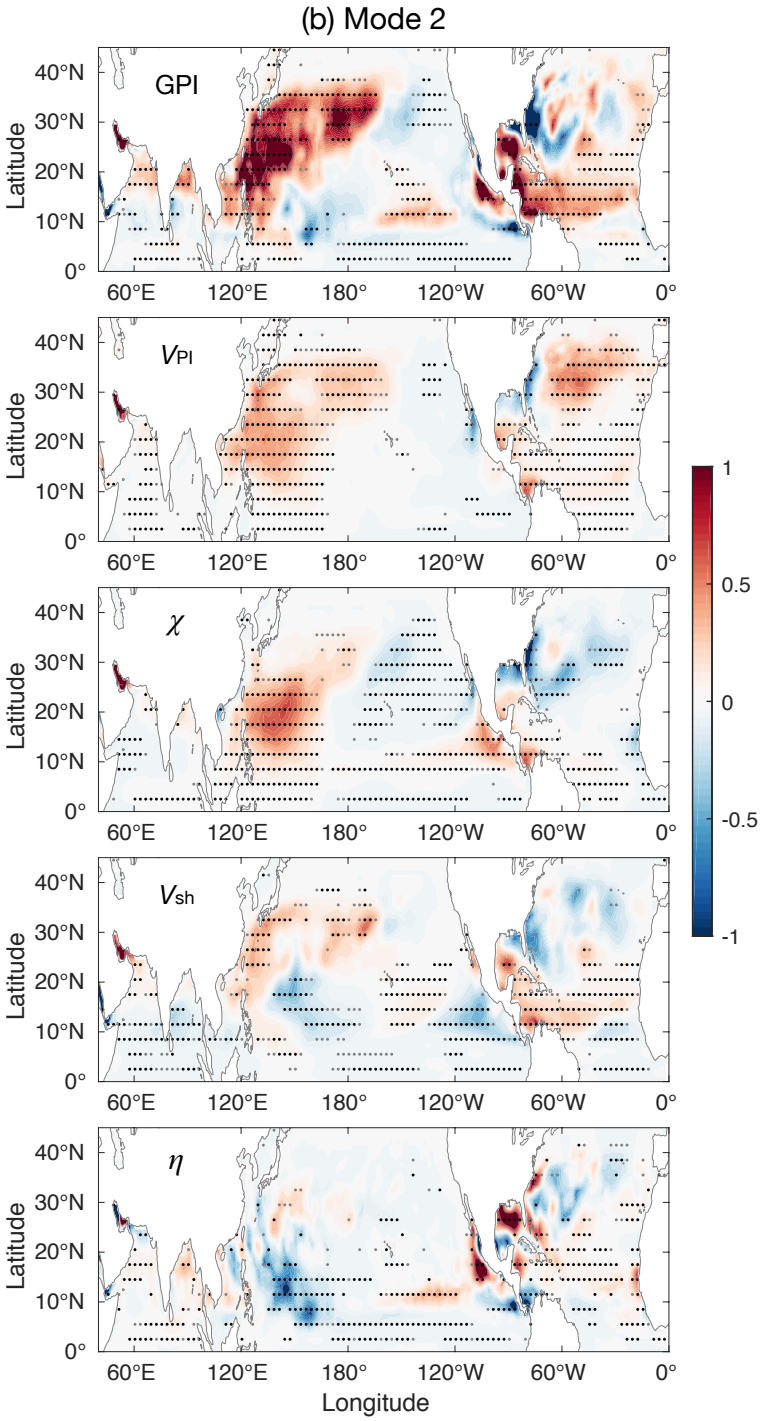

1110

1111 Fig. 5. (continued)

1112

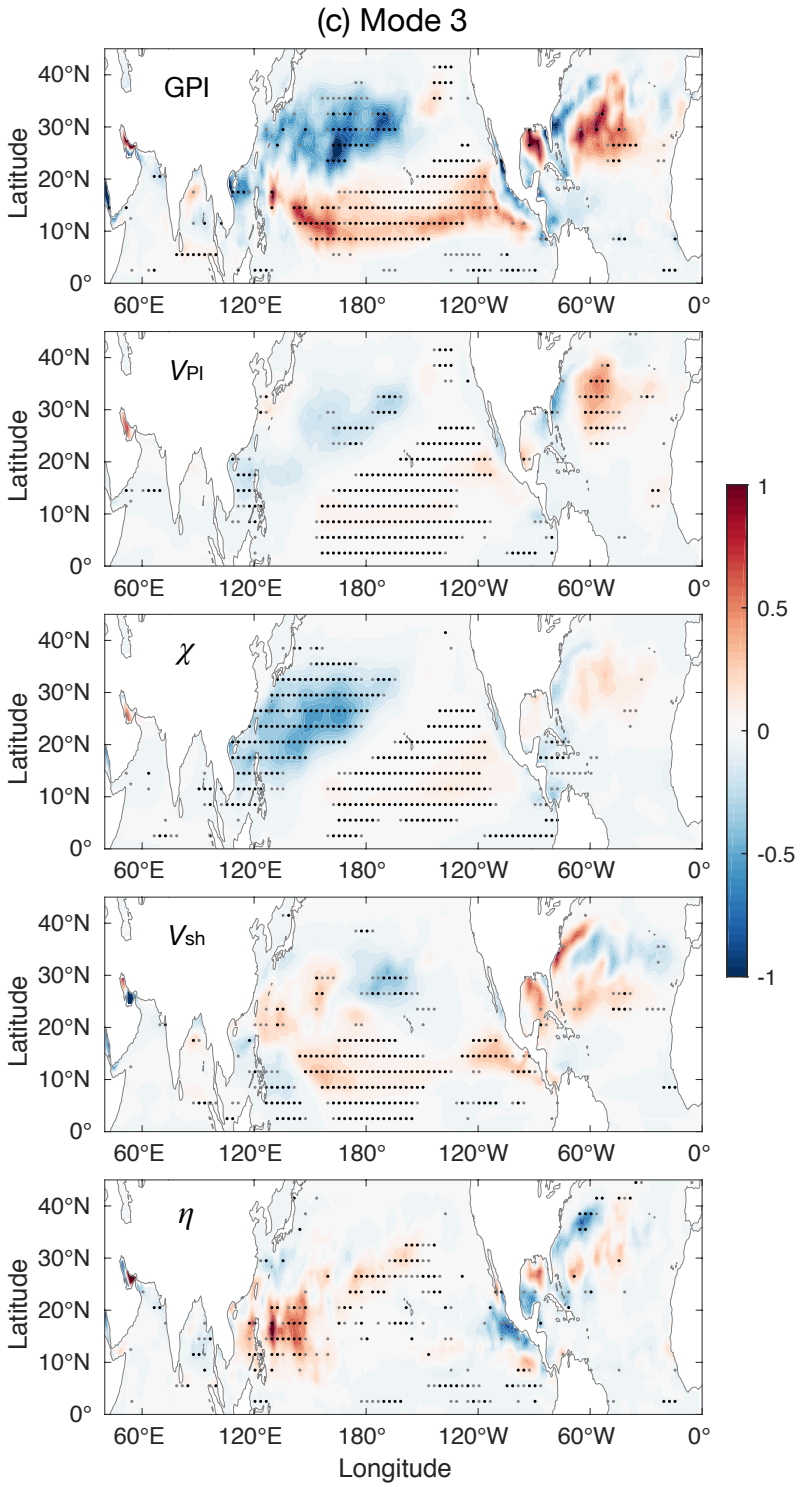

1113
1114 Fig. 5. (continued)

1115

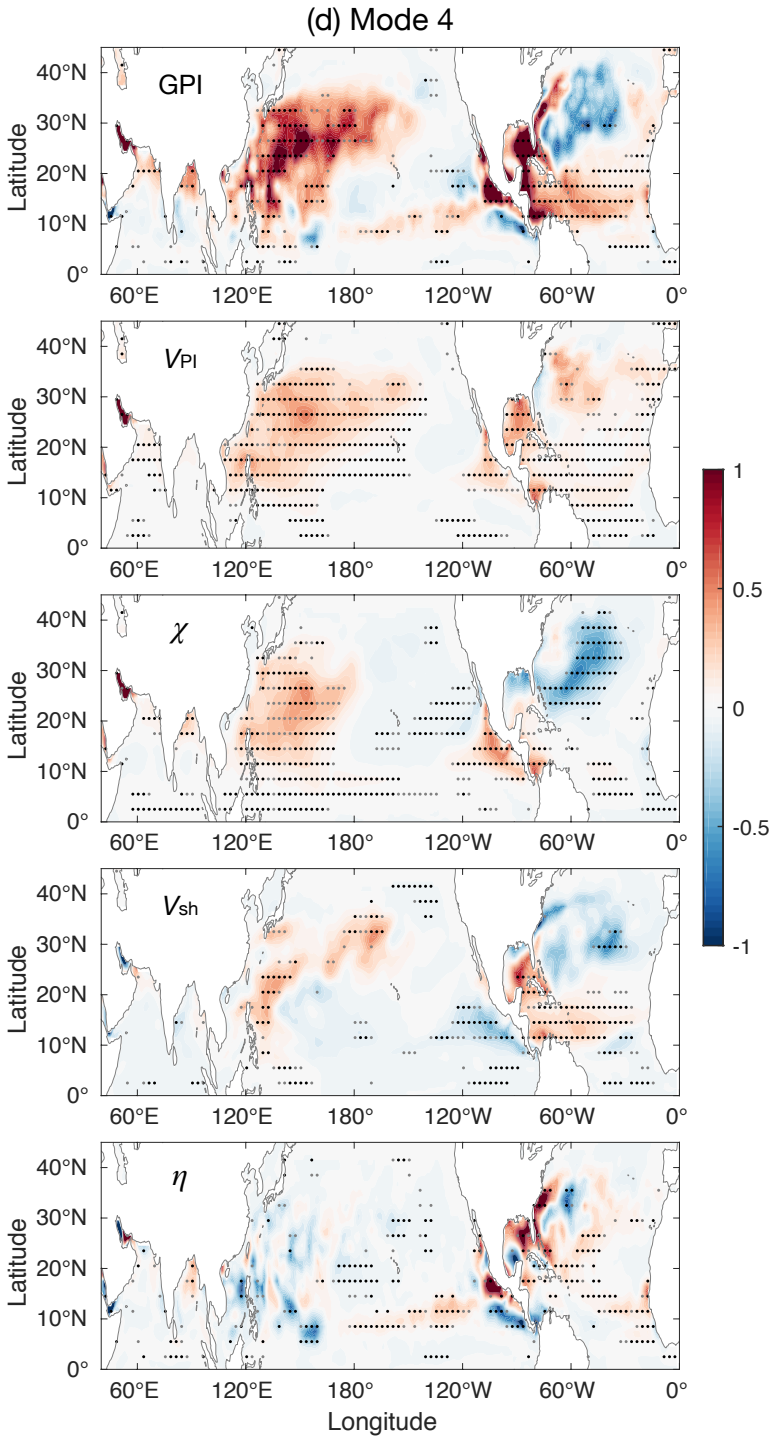

Fig. 5. (continued)

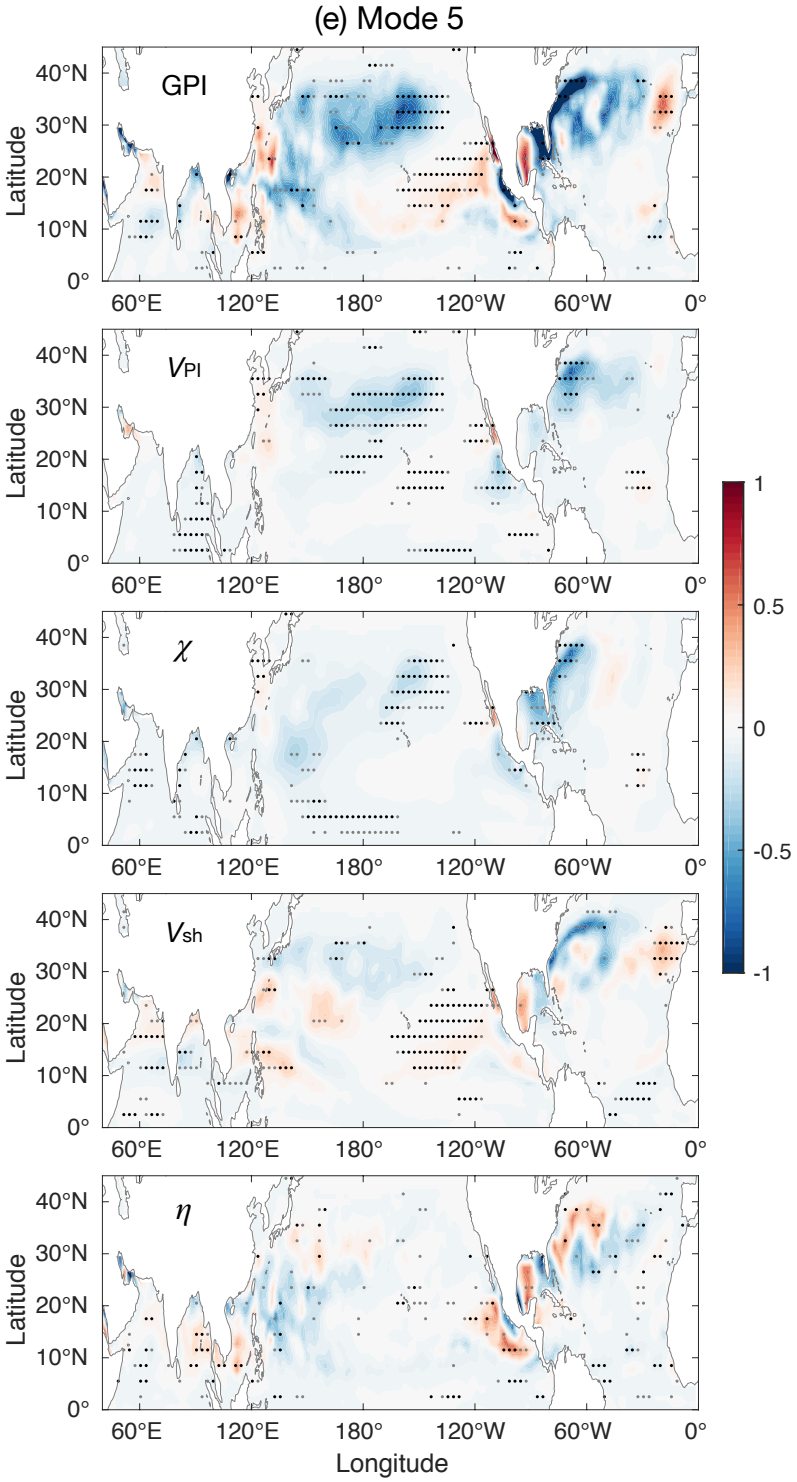

1119
1120 Fig. 5. (continued)

1121

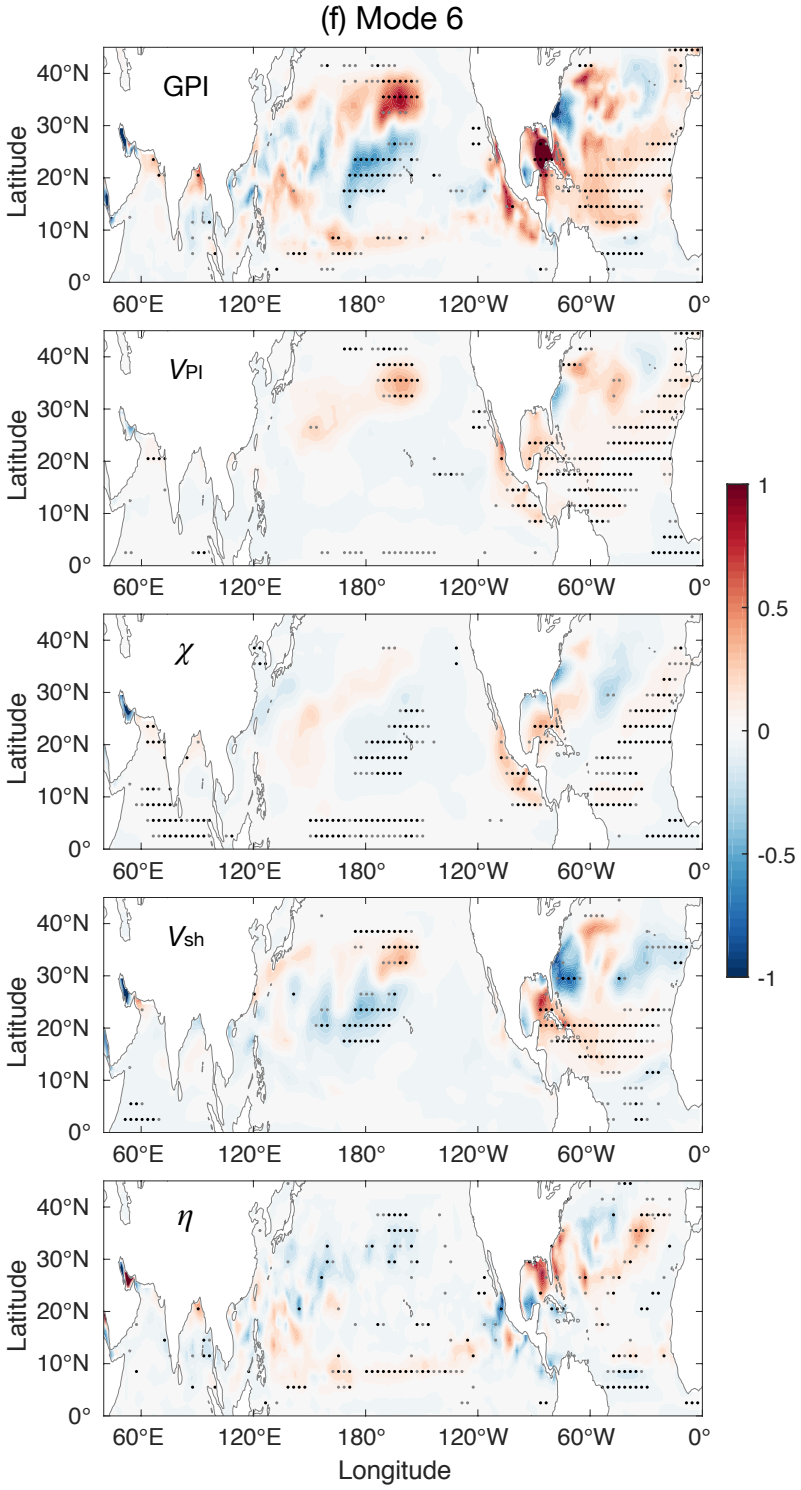

1122
1123 Fig. 5. (continued)

1124

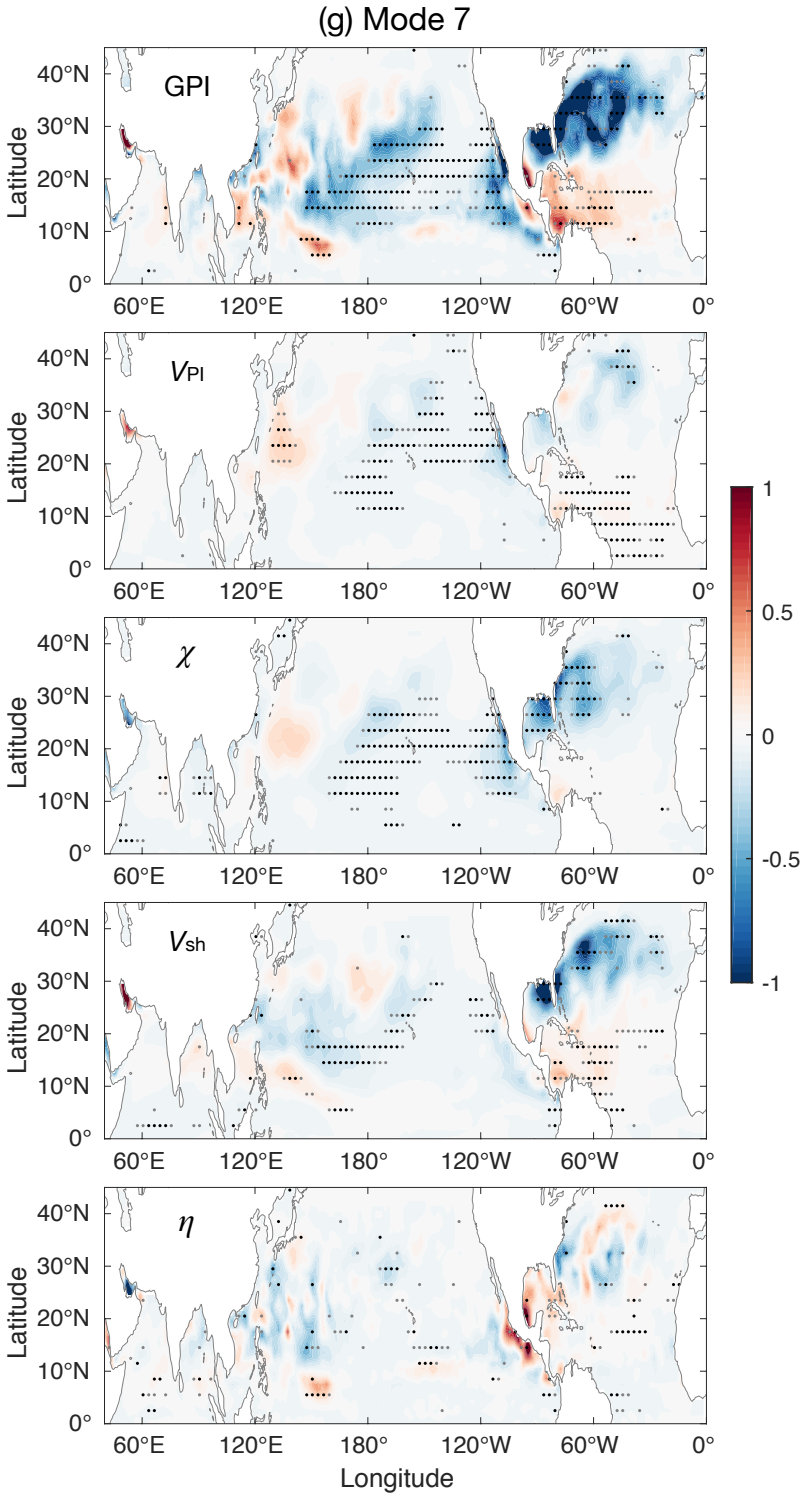

Fig. 5. (continued)

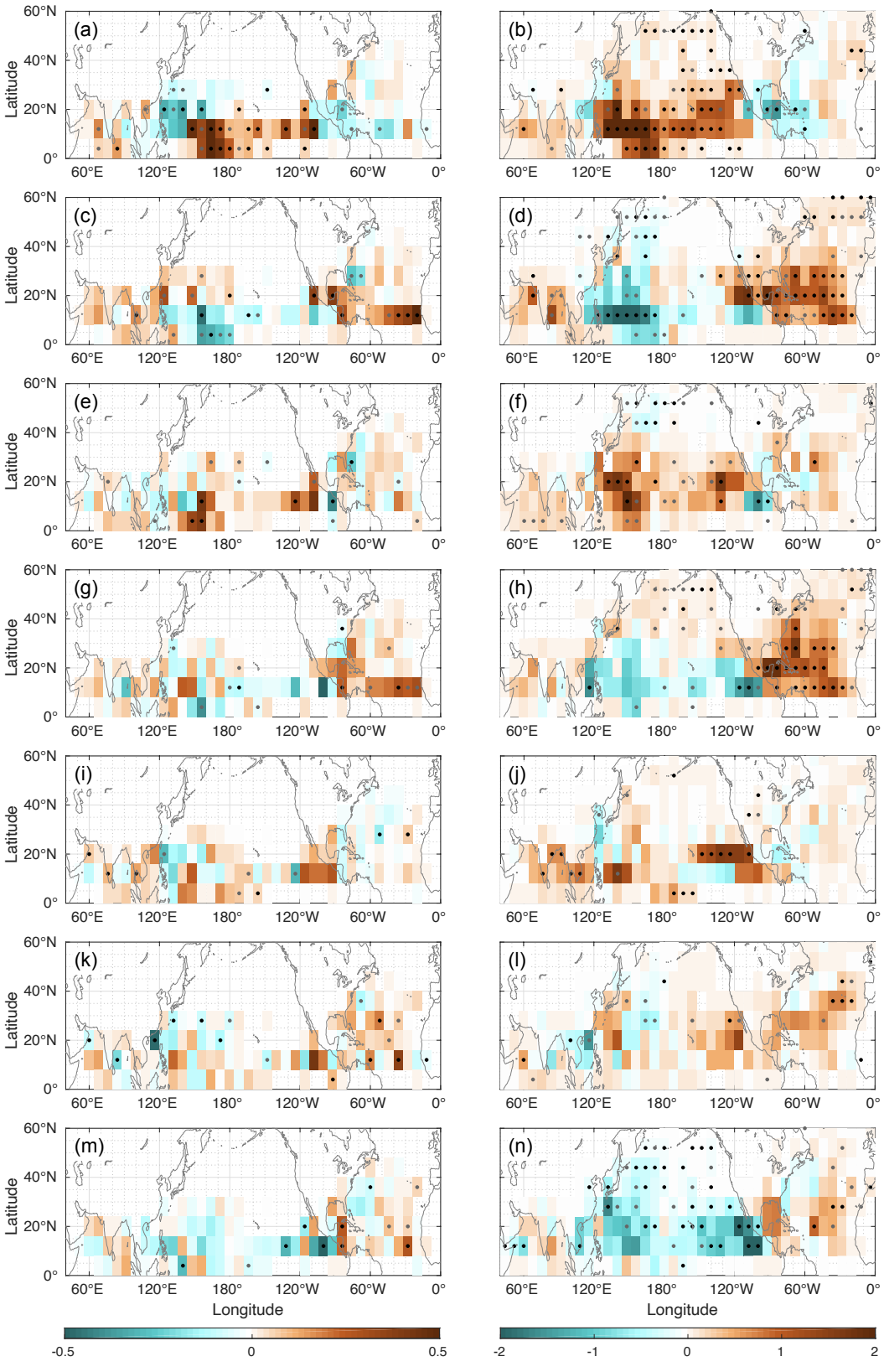
(a)
(b)
(c)
(d)
(e)
(f)
(g)
(h)
(i)
(j)
(k)
(l)
(m)
(n)
60°N
40°N
20°N
0°
Latitude
60°E
120°E
180°
120°W
60°W
0°
Longitude
-0.5
0
0.5
-2
-1
0
1
2

1129

Fig. 6. The regressed anomalies of TC genesis frequency (a,c,e,g,i,k,m) and occurrence frequency (b,d,f,h,j,l,n; unit: days) against the PC of M1 (a,b), M2 (c,d), M3 (e,f), M4 (g,h), M5 (i,j), M6 (k,l) and M7 (m,n) during 1969–2018. Black (grey) dots denote areas with regression coefficients significant at the 0.05 (0.1) level.

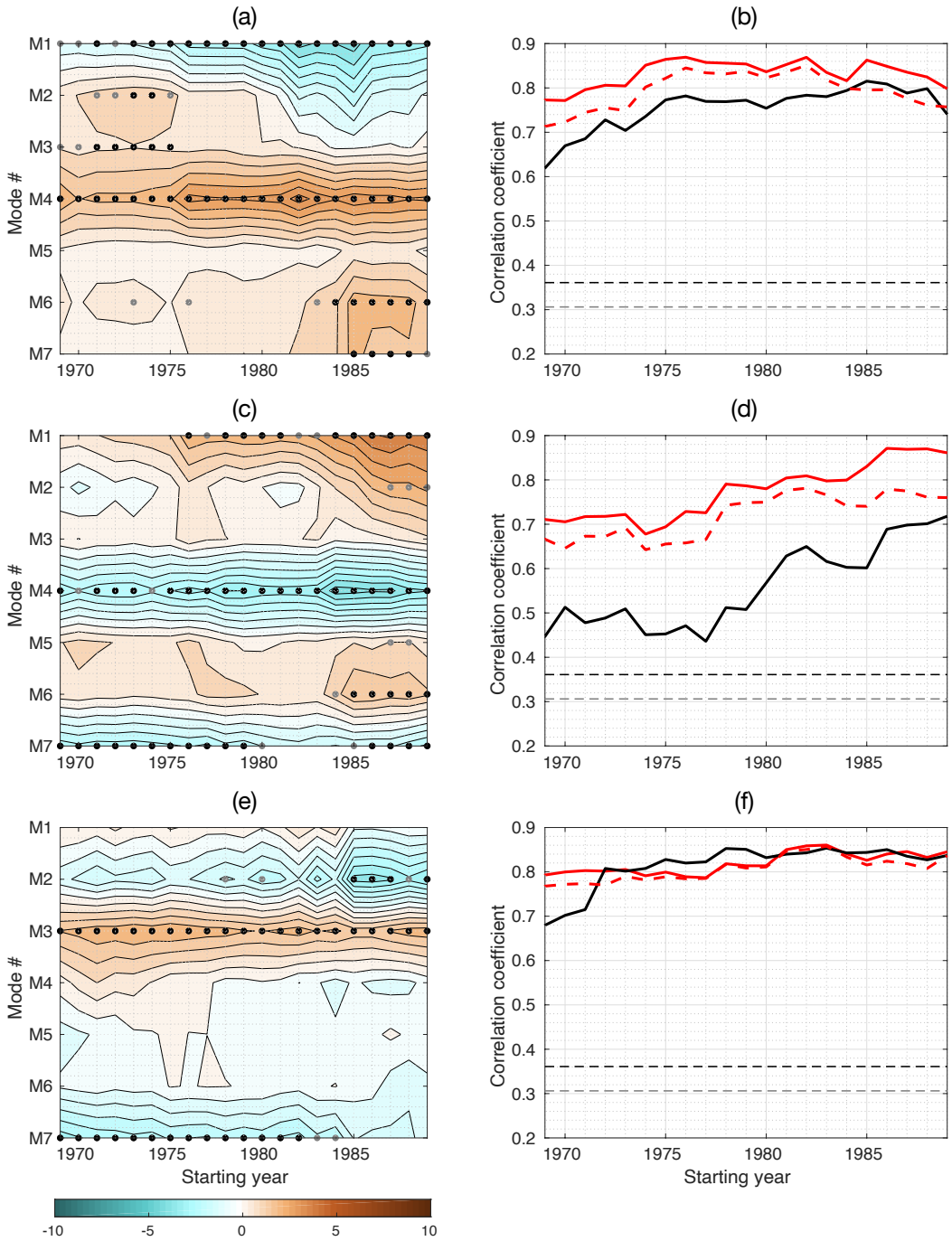

Fig. 7. (a,c,e) The coefficients for the PCs of M1–M7 from the multiple linear regression analysis of TCGF in the NA (a), NEP (c) and NWP (e) during various 30-year periods with the starting year sliding from 1969 to 1989 (i.e., 1969–1998, 1970–1999, …, 1989–2018). Black (grey) dots indicate that the regression coefficients are significant at the 0.05 (0.1) level. (b,d,f) The correlation skill of the TCGF reconstructed from the multiple linear regression using the PCs of M1–M7 (solid

red) and using six climate indices (solid black) for various 30-year period with the starting year sliding from 1969 to 1989 (i.e., 1969–1998, 1970–1999, …, 1989–2018). The six climate indices in use include Niño-3.4, global-mean SST, indices of the PMM, AMO, PDO and AMM. Dashed red curves show the correlation skill of the TCGF reconstructed using only PCs of the modes dominant in the basin (i.e., M1, M2, M4 and M6 for the NA; M1, M4 and M7 for the NEP; M2, M3 and M7 for the NWP). Thin dashed black (grey) horizontal line represents the threshold for a correlation coefficient significant at the 0.05 (0.1) level.